

REPORT DOCUMENTATION PAGE

Form Approved
OMB No. 0704-0188

Public reporting burden for this collection of information is estimated to average 1 hour per response, including the time for reviewing instructions, searching existing data sources, gathering and maintaining the data needed, and completing and reviewing the collection of information. Send comments regarding this burden estimate or any other aspect of this collection of information, including suggestions for reducing this burden, to Washington Headquarters Services, Directorate for Information Operations and Reports, 1215 Jefferson Davis Highway, Suite 1204, Arlington, VA 22202-4302, and to the Office of Management and Budget, Paperwork Reduction Project (0704-0188), Washington, DC 20503.

1. AGENCY USE ONLY (Leave Blank)	2. REPORT DATE	3. REPORT TYPE AND DATES COVERED
	December 1997	Final Technical Report 10/15/94 - 10/14/97

4. TITLE AND SUBTITLE	5. FUNDING NUMBERS
"Epitaxial Growth and Characterization of Si _{1-x} Ge _x Materials and Devices"	Grant # F49620-95-1-0013

6. AUTHORS	Pallab Bhattacharya
------------	---------------------

7. PERFORMING ORGANIZATION NAME(S) AND ADDRESS(ES)	8. PERFORMING ORGANIZATION REPORT NUMBER
Universty of Michigan Department of Electrical Engineering & Computer Science 1301 Beal Avenue Ann Arbor, MI 48109-2122	

9. SPONSORING / MONITORING AGENCY NAME(S) AND ADDRESS(ES)	10. SPONSORING / MONITORING AGENCY REPORT NUMBER
Air Force Office of Scientific Research 110 Duncan Avenue, Building 410 Bolling Air Force Base, DC 20332-6448	

11. SUPPLEMENTARY NOTES	
-------------------------	--

12a. DISTRIBUTION / AVAILABILITY STATEMENT	12b. DISTRIBUTION CODE
Approved for public release; distribution unlimited.	

13. ABSTRACT (Maximum 200 words)

The objectives of this project were the understanding of heteroepitaxial growth of SiGe/Si, dislocation control for highly mismatched layers, and the application of such heterostructures to high speed microelectronics and optoelectronics. A new technique of dislocation control, using a low-temperature Si buffer layer, has been identified. SiGe/Si heterostructure FETs have been fabricated, using this technique. Heterostructure bipolar transistors have been utilized to realize the first SiGe-based integrated photoreceivers. The electro-optic coefficients in SiGe/Si quantum wells have also been measured. Modulators, whose operation principle is based on the small conduction band offset, in this heterostructure, has been demonstrated theoretically and experimentally, for the first time. Theoretical work, involving a charge control study of the interfacial effects in p-MOSFETs.

DTIC QUALITY INSPECTED 2

14. SUBJECT TERMS	15. NUMBER OF PAGES
	36
	16. PRICE CODE

17. SECURITY CLASSIFICATION OF REPORT	18. SECURITY CLASSIFICATION OF THIS PAGE	19. SECURITY CLASSIFICATION OF ABSTRACT	20. LIMITATION OF ABSTRACT
UNCLASSIFIED	UNCLASSIFIED	UNCLASSIFIED	UNLIMITED

NSN 7540-01-280-5500

Standard Form 298 (Rev. 2-89)
Prescribed by ANSI Std. Z39-1
298-102

**EPITAXIAL GROWTH AND CHARACTERIZATION OF
Si_{1-x} Ge_x MATERIALS AND DEVICES**

AFOSR Grant No: F49620-95-1-0013

**Final Technical Report
for the Period:**

October 15, 1994 - October 14, 1997

Submitted to

**Dr. G. Witt
Air Force Office of Scientific Research/NE
Building 410
Bolling Air Force Base, DC 20332-6448**

by

P. Bhattacharya, J. Singh and E. Gulari

**Solid State Electronics Laboratory
Department of Electrical Engineering & Computer Science
The University of Michigan
Ann Arbor, Michigan 48109-2122
Telephone: 734-763-6678**

December 26, 1997

1. Introduction

Work in this project has focused on the development of SiGe/Si heterostructures for high-speed electronic and optoelectronic devices. We have studied the fundamental growth processes of SiGe alloys and have elucidated important properties of adatom migration during MBE that were hitherto unknown. We have characterized the use of a low temperature Si(LT-Si) buffer for producing defect-free SiGe epitaxy layers. We have fabricated strained Si n-MOSFETs grown on relaxed using the LT-Si buffer mechanism. Work is continuing to fabricate high-frequency SiGe/Si HBTs and photoreceiver circuits. We have also characterized high performance SiGe/Si electro-optic modulators. We have explored light emitting sources on Si using InAs/GaAs quantum dots. We also present a numerical formalism to address the band structure of *p*-type MOSFETs. The results in each of these areas are described in the following sections.

2. $\text{Si}_{1-x}\text{Ge}_x/\text{Si}$ System and Epitaxy Description

Growth is performed using a three-chamber RIBER-32 growth system as shown in Fig. 2.1. The three chamber system minimizes contamination in the growth chamber which might occur during sample loading. An electronically controlled shutter provides quick on-off times for each port. An LN_2 cryoshroud is used to prevent the active solid cells from overheating. Ultra-high vacuum conditions(10^{-10} Torr) maintained during growth using a turbomolecular pump(2200l/s), backed by a mechanical pump; an ion pump is used during idle periods. *In-situ* surface monitoring is obtained by reflection high energy electron diffraction(RHEED). The chamber is also equipped with a pulsed supersonic valve for producing very high *n*-type doping concentrations($\geq 10^{19}\text{cm}^{-3}$)[1]. Pure disilane and phosphine(1% in H_2) are used as gas sources. Solid source germanium(Ge) and Boron(B) are also used as source materials.

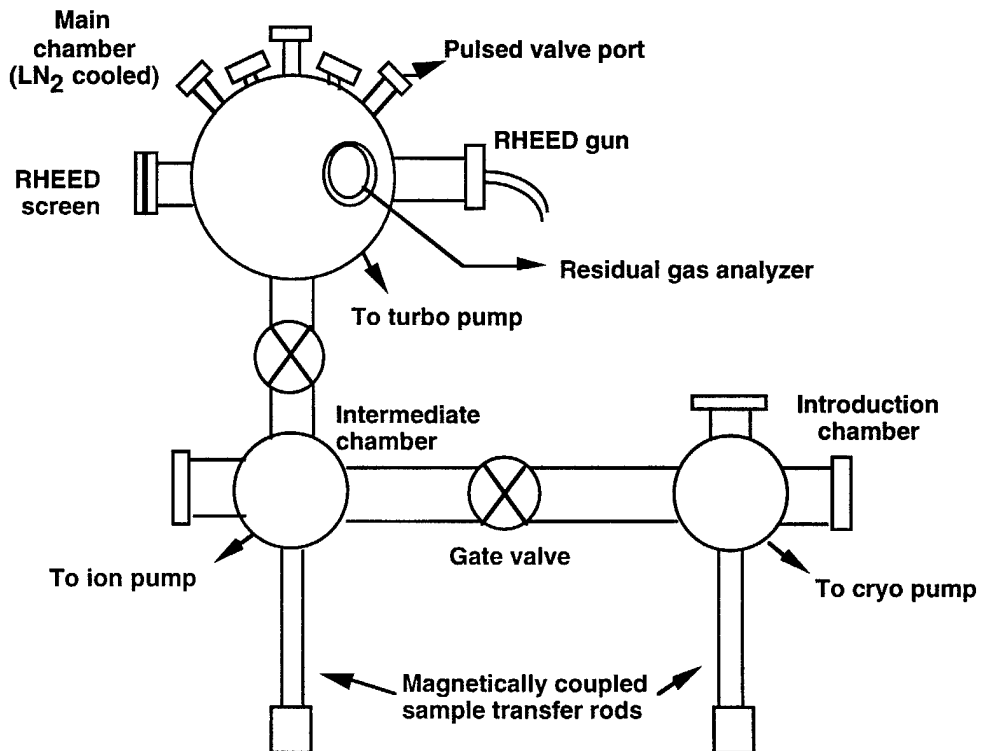


Figure 2.1. Schematic of three chamber RIBER-32 growth system

3. Kinetics of $\text{Si}_{1-x}\text{Ge}_x/\text{Si}$ ($0 \leq x \leq 1$) Growth by Molecular Beam Epitaxy Using Disilane and Germanium

Two series of $\text{Si}_{1-x}\text{Ge}_x$ layers were grown. In the first, the Ge content was varied by keeping the Ge cell temperature constant at 1120°C and varying the Si_2H_6 flow rate, with an MKS mass-flow controller, in the range of 0 to 55 sccm. In the second set of samples, the Ge content was varied by holding the Si_2H_6 flow rate constant at 14 sccm and varying the Ge cell temperature in the range of $1000-1200^\circ\text{C}$. It may be noted that all the layers were strain relaxed, their thickness being larger than the critical thickness. The alloy composition was determined by double-crystal x-ray measurements, using $\text{CuK}\alpha_1$ line, and was confirmed by RBS measurements.

Figures 3.1(a) and (b) show the variation of growth rate with Ge content in the alloy for the two methods of growth. In the first case, when the Ge cell temperature, or flux, is held constant, the growth rate monotonically decreases with Ge content in the alloy. However, when the composition is varied by varying the Ge flux, as shown in Fig. 3.1(b), the growth rate first decreases and then increases sharply. It is important to note that growth rate data for alloys with high Ge content ($x \geq 0.4$) have not been hitherto reported.

The growth behavior indicated by Fig. 3.1(a) is easily understood. As the Si_2H_6 flow rate is decreased, the Ge content in the alloy increases, but the growth rate decreases. The growth phenomenon represented by the data of Fig. 3.1(b) is more interesting. Here the Si_2H_6 flow rate maintained constant, and the different alloy compositions are obtained by varying the Ge flux. One would expect that the growth rate initially decreases up to $x=0.5$ and then increases. A curve-fitting indicates that the measured data can be the sum of two curves, one decreasing slowly with x (shown in Fig. 3.1(b) by the dashed line) and the other increasing with x (shown in Fig. 3.1(b) by the dot-dashed line). The latter represents the increase of growth rate with increasing Ge flux. The curve however would suggest that there is actually a surface phenomenon that tends to *decrease* the growth rate with increasing Ge flux. From the measured growth rates as a function of x , it is clear that the presence of Ge tends to decrease the Si incorporation rate. This establishes growth via migration to kink sites in a dissociative chemisorption process.

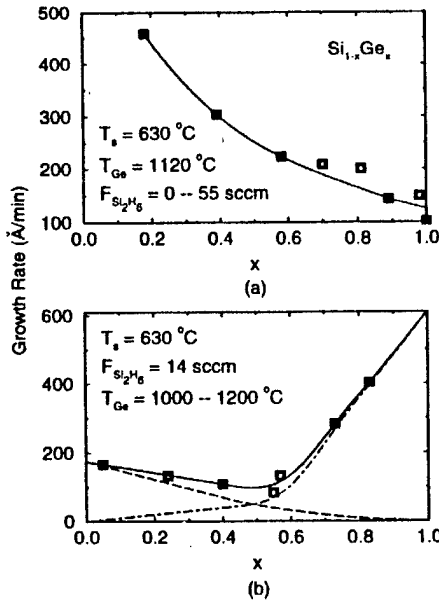


Figure 3.1 $\text{Si}_{1-x}\text{Ge}_x$ layer growth rates as a function of Ge fraction for two growth methods: (a) the Ge cell temperature is held constant at 1120°C and the Si_2H_6 flow rate is varied; (b) the Si_2H_6 flow rate is held constant at 14 sccm and the Ge cell temperature is varied.

4. Low Temperature Si Buffer Layers and its Impact on Heteroepitaxy

4.1 Introduction

One of the obstacles of producing defect-free $\text{Si}_{1-x}\text{Ge}_x$ epitaxy is the generation of misfit dislocations due to strain relaxation at the substrate/epitaxy interface. The 4% lattice mismatch between Si and Ge is compensated by an increase in the strain energy at the $\text{Si}_{1-x}\text{Ge}_x/\text{Si}$ interface, resulting in the growth of a pseudomorphic crystal. Above the critical thickness, threading dislocations form in the $\text{Si}_{1-x}\text{Ge}_x$ layer which can degrade material quality resulting in poor device performance[2]. Several authors have used superlattice and step-graded layers to reduce the threading dislocation density producing mixed results[2-9]. Such methods require fairly thick layers($\sim 1\mu\text{m}$) which can contribute to poor lithography.

Several authors have been successful in producing defect-free epitaxy using either amorphous, polycrystalline, and low-temperature buffer layers. Chen et al. has reported significant dislocation reduction in bulk $\text{Si}_{1-x}\text{Ge}_x$ layers using a low temperature Si buffer[10]. Amano et al. has had amazing success producing defect-free GaN films for ultraviolet laser diodes using a low temperature AlN buffer layer[11]. We have investigated the use of a low temperature Si(LT-Si) buffer for reducing the threading dislocation density in relaxed $\text{Si}_{1-x}\text{Ge}_x/\text{Si}$ heterostructures.

4.2 Results and discussion

For our LT-Si study, an initial Si buffer was grown at 700°C followed by a $0.1\mu\text{m}$ thick LT-Si layer grown at 450°C . A $0.5\mu\text{m}$ thick $\text{Si}_{0.85}\text{Ge}_{0.15}$ was then grown under normal growth conditions at 570°C . In comparison, a control was grown which consisted of an initial Si buffer followed by a $0.5\mu\text{m}$ thick $\text{Si}_{0.85}\text{Ge}_{0.15}$ grown under normal growth conditions.

XTEM micrographs of heterostructures without and with the LT-Si buffer layer, as shown in Figs. 4.1(a) and (b), respectively, indicate that most or all of the threading dislocations are contained below the SiGe/LT-Si interface. Because there are no threading dislocations in the micrograph provided, one can conclude that the total number of dislocations in the bulk SiGe layer is at most 10^4cm^{-2} [6]. In the sample without the LT-Si buffer, the threading dislocations propagate to the $\text{Si}_{1-x}\text{Ge}_x$ layer surface, as expected.

Another study was conducted comparing the efficacy of the LT-Si buffer defect reduction mechanism with $\text{Si}_{1-x}\text{Ge}_x$ layers of different Ge compositions. The samples were grown on p^+ (100)-oriented Si substrates by ultra-high vacuum chemical vapor deposition(UHV-CVD). Germane(10% in helium) and ULSI-grade silane(100%) were used as gas sources. The sample consist of a $0.2\mu\text{m}$ thick LT-Si buffer grown at 425°C followed by a $0.7\mu\text{m}$ thick $\text{Si}_{0.7}\text{Ge}_{0.3}$ and $\text{Si}_{0.6}\text{Ge}_{0.4}$, respectively, grown under normal growth temperatures at 525°C . Bright field (200) cross-section imaging indicates a near defect free SiGe region, as shown in Fig. 4.2(a). Bright field plan-view(022) imaging of the same sample, shown in Fig. 4.2(b), indicates that the dislocation network is contained within the LT-Si buffer layer. For higher Ge(>40%) composition samples, as shown in Fig. 4.2(c), optimization of the LT-Si buffer layer for higher Ge composition alloys is still under investigation.

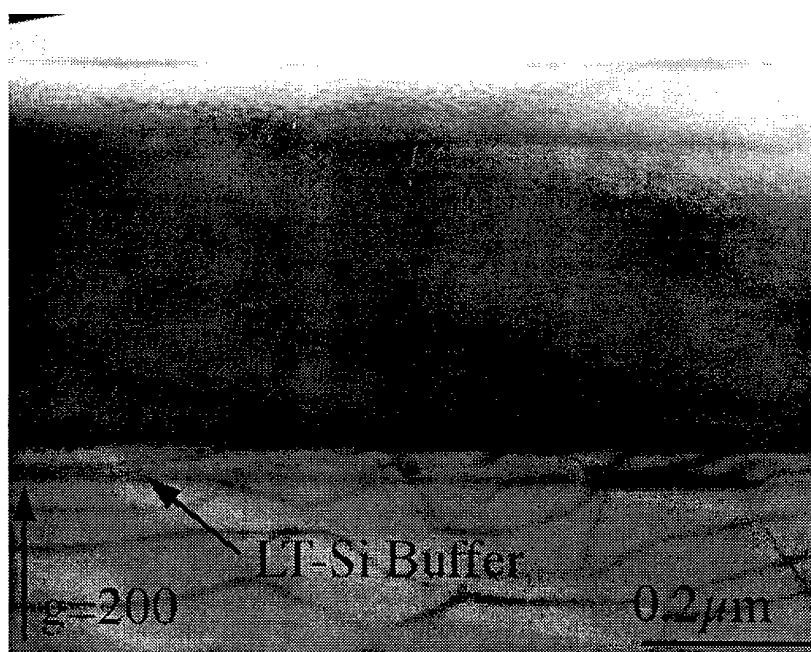
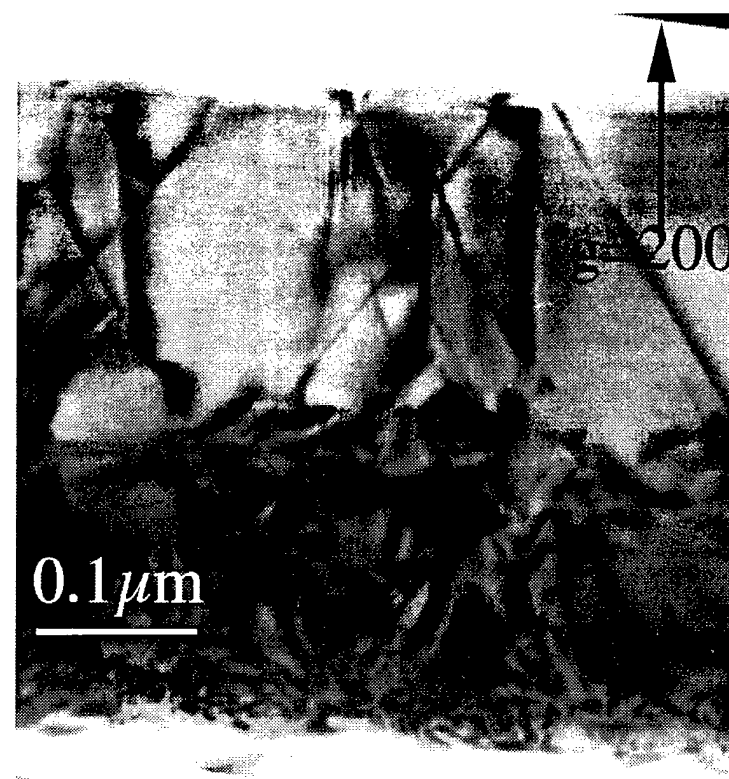


Figure 4.1. Bright-field(200) cross-section TEM images for $0.5\mu\text{m}$ $\text{Si}_{0.85}\text{Ge}_{0.15}$ grown on Si: (a) without and (b)with LT-Si buffer.

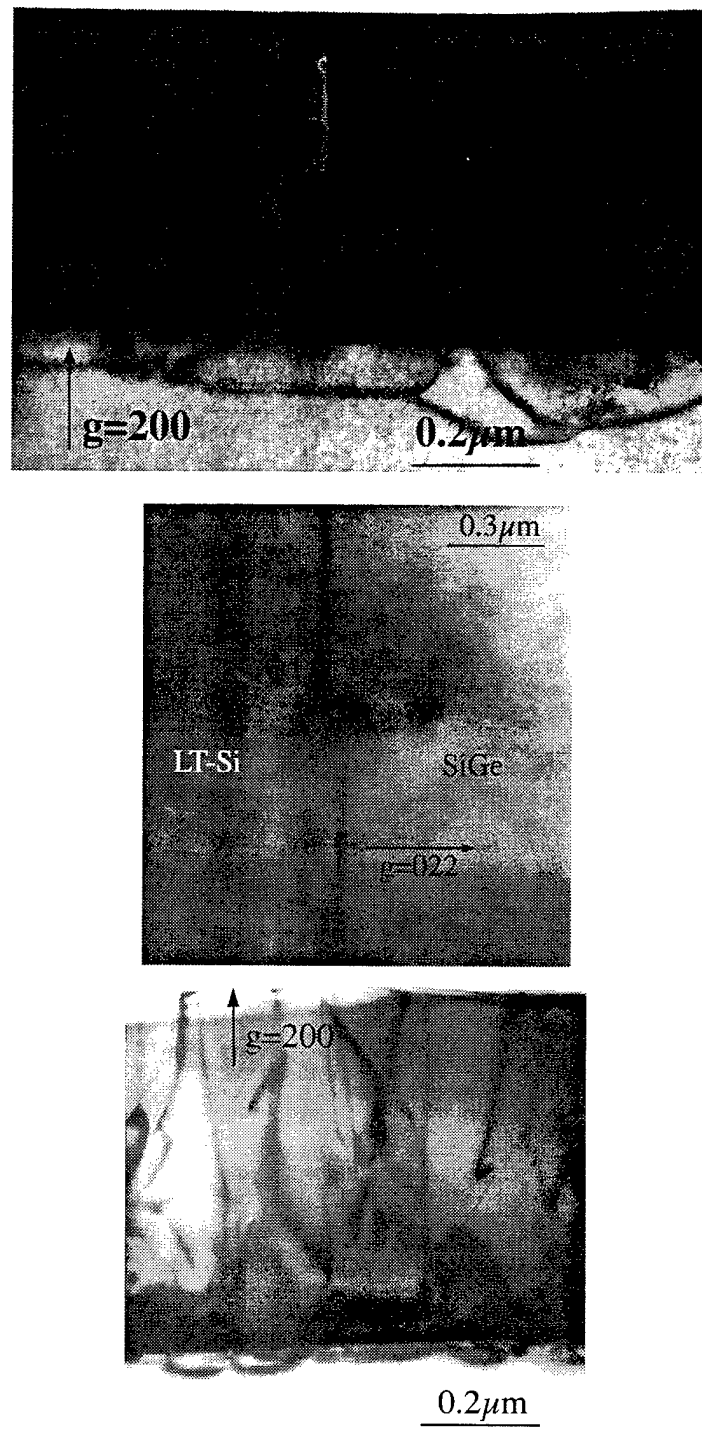


Figure 4.2. (a)Cross-section and (b)plan-view TEM images of a $0.7\mu\text{m}$ $\text{Si}_{0.7}\text{Ge}_{0.3}$ layer grown on a $0.2\mu\text{m}$ LT-Si buffer layer. (c) shows the cross-section of a $\text{Si}_{0.6}\text{Ge}_{0.4}$ layer

Double crystal x-ray measurements of the $\text{Si}_{0.85}\text{Ge}_{0.15}$ layer without and with the LT-Si buffer layer indicate that the width(FWHM) of the rocking curve corresponding to the alloy peak is reduced from 450 arc seconds to 371 arc seconds, respectively. Hall measurements were performed at room temperature on $1\mu\text{m}$ thick $\text{Si}_{0.7}\text{Ge}_{0.3}$ layers grown with and without the LT-Si buffer layer. The samples were boron doped at $3.4\pm1.8\times10^{17}\text{cm}^{-3}$. Ohmic contacts were made from indium dots annealed at 400°C for 10 minutes. Hole mobility improved from $160\pm18\text{cm}^2\text{V}^{-1}\text{s}^{-1}$ to $200\pm2.5\text{ cm}^2\text{V}^{-1}\text{s}^{-1}$ by incorporating the LT-Si buffer layer. The mechanism for threading dislocation reduction is still under investigation. We suspect that because of the low growth temperature, a large number of point defects are generated in the LT-Si buffer layer. As the misfit dislocations propagate through the LT-Si layer, they become trapped by the defects and are annihilated.

From Fig. 4.1(b), one should note the existence of threading dislocations in the substrate region just below the LT-Si buffer layer. We believe that the threading dislocations found deep inside the substrate are generated from the activation of modified Frank-Read sources which can relieve the strain in the SiGe epilayer[12]. The bowing mechanism is also observed in samples using graded layers and superlattices to relieve strain [6,13].

4.4 Conclusion

We have investigated a new defect density reduction method for SiGe heterostructures which uses an LT-Si buffer layer. Both gas-source MBE and UHV-CVD technologies have demonstrated threading dislocation densities as low as 10^4cm^{-2} . Preliminary SiGe/Si n-p-n HBTs exploiting the LT-Si buffer layer have been grown and fabricated.

5. Strained Si *n*-MOSFETs Grown on Relaxed $\text{Si}_{1-x}\text{Ge}_x$ Using a Low Temperature Si Buffer

5.1 Introduction

Pseudomorphic strained Si n-MOSFETs grown on relaxed $\text{Si}_{1-x}\text{Ge}_x$ layers have recently demonstrated higher electron mobilities than bulk Si due to the lifting of the conduction band degeneracy at the $\text{Si}_{1-x}\text{Ge}_x/\text{Si}$ interface[14,15]. Intervalley scattering in the valence band is also reduced because of the increased separation between the split-off and valence bands, resulting in higher hole mobilities in strained Si p-MOSFETs[16]. The staggered Type-II junction formed at the tensile strained $\text{Si}_{1-x}\text{Ge}_x/\text{Si}$ interface also improves carrier confinement in the Si channel, which is otherwise difficult due to the near-zero conduction band offset in these heterostructures.

5.2 Results and discussion

Schematics of the strained Si and conventional Si n-MOSFETs are shown in Figures 5.1(a) and 5.1(b). The corresponding band diagram of the strained Si device, shown in Figure 4(c), shows a conduction band offset of 150meV. The devices were grown on p(100) substrates by UHV-CVD. The initial $0.2\mu\text{m}$ Si buffer for both devices was grown under normal growth conditions at 525°C . The control device contained an additional $0.7\mu\text{m}$ epitaxy Si layer grown under normal growth conditions. For the strained Si device, an $0.2\mu\text{m}$ LT-Si buffer was grown at 450°C followed by a $0.7\mu\text{m}$ $\text{Si}_{0.8}\text{Ge}_{0.2}$ layer and a 12nm Si channel . Relaxation of the $\text{Si}_{0.8}\text{Ge}_{0.2}$ layer was confirmed by X-ray diffraction.

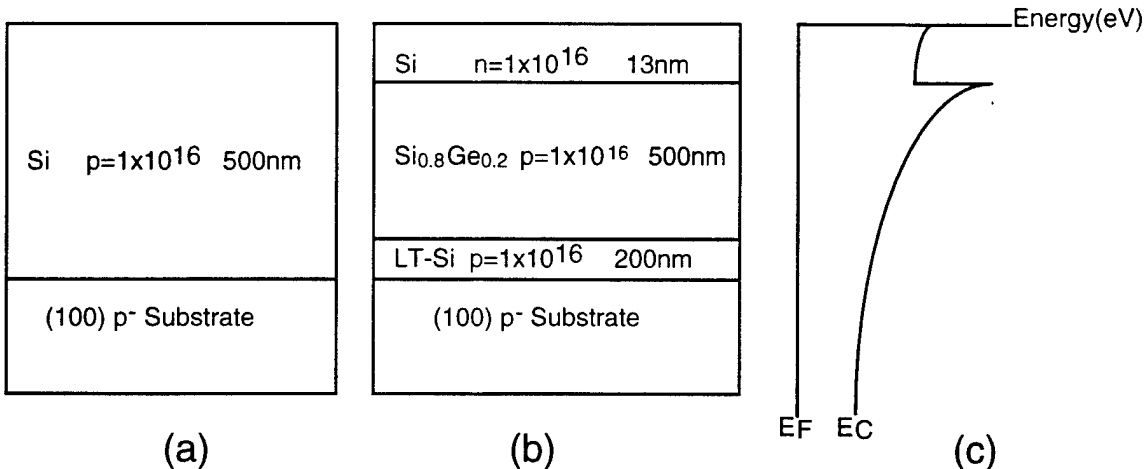


Figure 5.1 Schematic of (a) conventional Si n-MOSFET, (b) strained Si n-MOSFET, and (c) the corresponding band diagram of device (b).

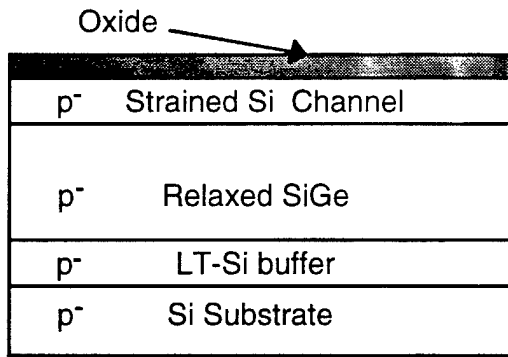
Dry oxidation, using a Limbergh furnace, was used to form the gate oxide. The samples were cleaned using a modified Piranha clean which includes a 15 min. emulsion in $\text{H}_2\text{O}_2:\text{H}_2\text{SO}_4$ (1:1) followed by a 3 min. cascade rinse. Native oxide removal was performed in a HF:DI H_2O (1:10) solution for 30 sec. The samples were immediately placed in the furnace. The gate oxide (~12nm) was then grown at 750°C for 120 min. followed by 10 minute anneal in N_2 gas ambient.

The oxide thickness had to remain below 12nm whereas not to consume the entire Si channel during oxidation. Calibration of the oxide thickness was obtained using capacitance-voltage(C-V) measurements. The samples were n^+ (100)-oriented Si substrates with resistivities between 0.008-0.02Ω-cm. After oxidation, the samples were patterned by Cr/Au (500/2500Å) metallization. Oxide removal was performed on the unmetallized substrate by a 30 second BHF dip; the substrate was then used as a contact.

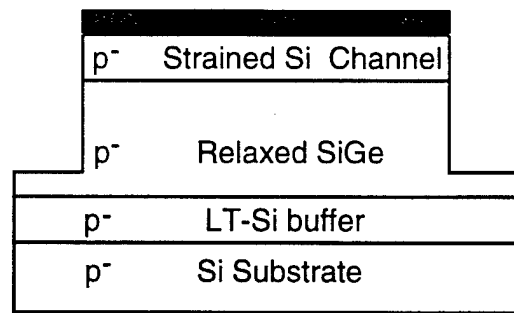
Figure 5.2 shows a schematic of the device fabrication process. Dry-etched mesas were used for device isolation. Phosphorus ion implants were used to define the source/drain regions($6 \times 10^{14} \text{ cm}^{-2}$, 25keV). A two-step low temperature anneal is used for implant activation((i)550°C for 40 min. to repair damaged Si and (ii)750°C for 20 min. to activate dopants). A sheet resistance of $2 \times 10^5 \Omega\text{-cm}$ was obtained. Pure Al(2500Å) is evaporated for ohmic contacts and annealed at 450°C for 15 minutes in forming gas. Cr/Au(500/2500Å) metallization is used to define the gate metal.

Typical I-V characteristics of the strained Si n-MOSFET are shown in Fig. 5.3(a). From the output characteristics of 1μm gate transistors, we find that peak high-field transconductance, g_m , is 14mS/mm, 20mS/m and 25mS/mm respectively, for the conventional MOSFET, the MOSFET with graded $\text{Si}_{1-x}\text{Ge}_x$ buffer, and the MOSFET with the LT-Si buffer layer. Cutoff is ~1V. A comparison of g_m for the conventional Si and strained Si n-MOSFET and are shown in Fig. 5.3(b). The low current is due to the low carrier density in the channel. High current resistivity is reflected in the high saturation at voltage($V_{DS}=5\text{V}$) at $V_G=3.0\text{V}$. Similar results were obtained from the conventional Si device. After increasing the implant energy to 100keV, we found lower sheet resistance; the saturation voltage, at $V_G=3.0\text{V}$, reduced to $V_{DS}=3\text{V}$. The effective electron mobility, $\mu_{eff}=(\partial I_{DS}/\partial V_{GS})(L/W)(V_{DS}C_{OX})$ indicates a higher maximum mobility of $711\text{cm}^2/\text{Vs}$ for the strained n-MOSFET with the LT-Si buffer layer compared to $248\text{ cm}^2/\text{Vs}$ with conventional Si n-MOSFET.

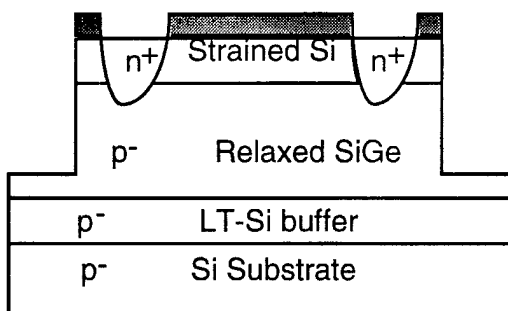
1. Oxide growth



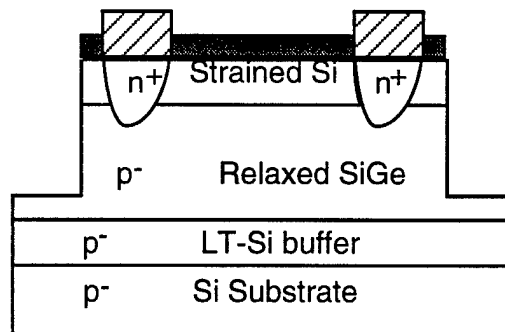
2. Mesa etch



3. Ion Implantation



4. Ohmic metal evaporation



5. Gate metal evaporation

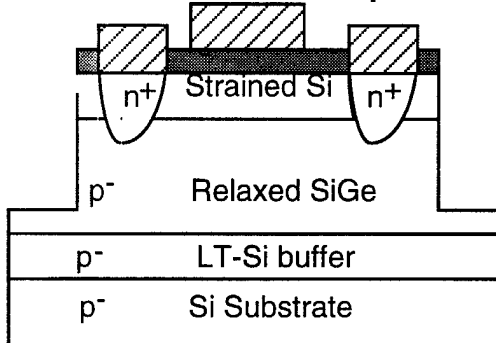


Figure 5.2. Schematic of device fabrication process

5.3 Conclusion

We have fabricated strained Si n-MOSFETs grown on relaxed $\text{Si}_{1-x}\text{Ge}_x$ alloys exploiting the LT-Si buffer defect reduction mechanism. A comparison between strained Si and conventional Si devices indicates that device performance is enhanced with the strained Si channel. Fabrication of submicron gate devices is currently being investigated.

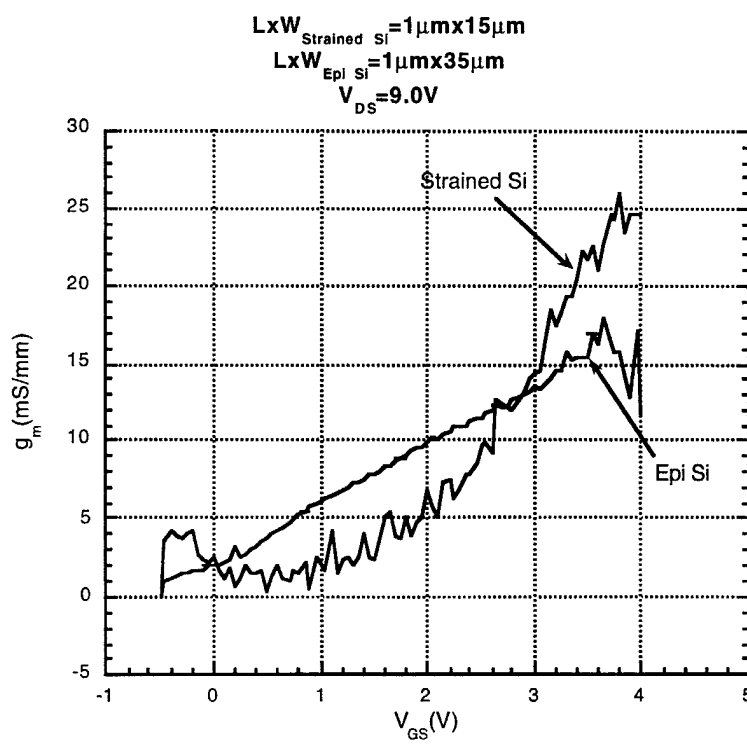
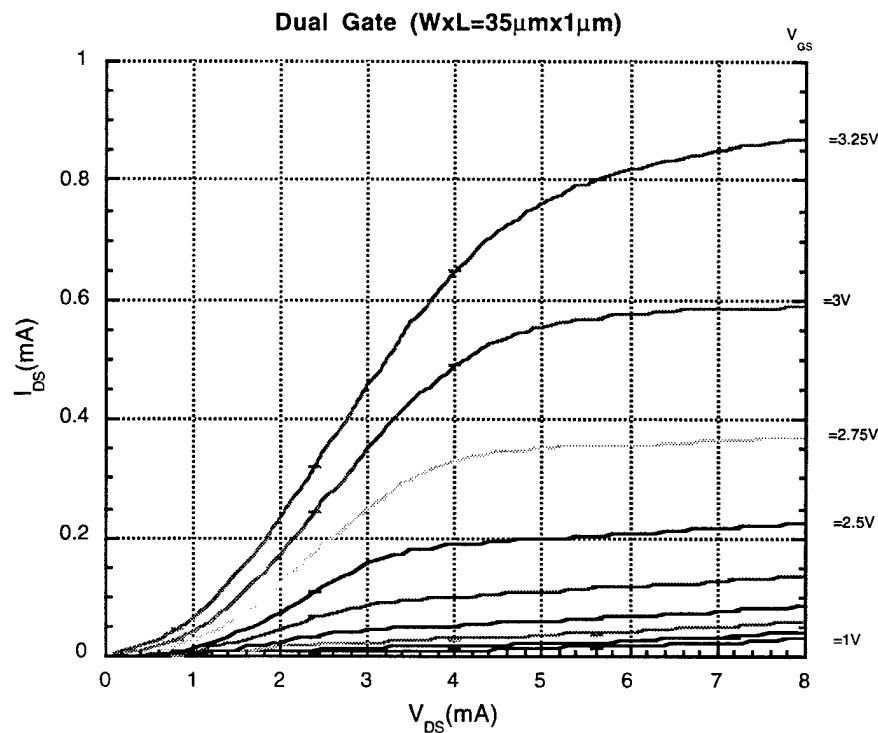


Figure 5.3. (a)I-V characteristics of strained Si n-MOSFETs. (b) A comparison of transconductance performance between strained Si and conventional Si n-MOSFETs.

6. Monolithically Integrated SiGe/Si PIN-HBT Front-End Transimpedance Photoreceivers

6.1 Introduction

The commercial market for optical communication keeps expanding as modern society requires faster communication systems with higher capacity. In a large scale, long-haul fiber optical communication is spreading quickly and is ready for penetration into homes and offices. In a small scale, local optical data link is expected to replace electrical interconnection for high-speed computation and switching application[17]. As a result, the demand for components comprising optical communication systems is rising rapidly. To meet this huge demand, mass production is necessary and this requires a technology with low cost and high reliability. Till date, III-V based technology has primarily dominated these applications owing to its high-speed characteristics, superior optical properties, and feasibility to incorporate materials corresponding to $1.3\text{ }\mu\text{m}$ and $1.55\text{ }\mu\text{m}$ wavelength, which are required for long-haul fiber optical communication system based on silica optical fibers in terms of low dispersion and low loss, respectively. The high-cost nature of III-V technology, however, remains a major impediment for it to be a favorable candidate for growing commercial applications which requires mass production. In contrast, Si-based technology benefits from its low cost and high reliability which is essential for commercial applications. There has been a lot of efforts to implement optical system components with Si technology, mainly for receiver modules. Such efforts started with hybrid approaches that combines III-V based photodiode to Si-based transimpedance amplifiers to make advantage of optical and high-speed properties of III-V materials and low cost nature of Si technology[18][19]. This approach, however, still suffers from its complexity and unreliability. Monolithic photoreceivers based on silicon, which eliminate the shortcomings of the hybrid realized by incorporating both photodiode and transimpedance amplifier on one chip, have been reported recently[20-23]. If the SiGe/Si heterostructure technology is incorporated to this monolithic approach, more advantages can be expected. SiGe/Si technology offers superior high speed characteristics than Si technology does, and it may be compatible with $1.3\text{ }\mu\text{m}$ and $1.55\text{ }\mu\text{m}$ wavelength by proper choice of Ge mole fraction in SiGe alloys while keeping the cost still low because it is basically based on existing matured Si technology. To the authors' knowledge, no SiGe based monolithic photoreceiver has been yet reported. In this paper, we report the development of SiGe/Si PIN-HBT technology and demonstrate the performance characteristics of transimpedance amplifiers and monolithically integrated PIN-HBT front-end transimpedance photoreceivers based on SiGe/Si heterostructures.

6.2 Fabrication

The schematic of the SiGe/Si PIN-HBT structure is shown in Fig. 6.1. A thick arsenic-doped subcollector layer is grown by CVD on (100) Si wafer with high resistivity ($\rho>2000\text{ }\Omega\text{cm}$). Then the wafer is loaded into the MBE chamber, and antimony-doped Si collector layer, boron-doped $\text{Si}_{1-x}\text{Ge}_x$ base layer, and antimony-doped Si emitter and emitter contact layer are grown. Unintentionally doped spacer layers are inserted in both sides of base to minimize the effect of boron out-diffusion. Ge mole fraction in the $\text{Si}_x\text{Ge}_{1-x}$ alloy incorporated as a base layer is graded from

Emitter Contact	Si	n+	1e19	200 nm
Emitter	Si	n	2e18	100 nm
Spacer	Si_{0.9}Ge_{0.1}	i		1 nm
Base	Si_{1-x}Ge_x x:0.1→0.4	p+	5e19	30 nm
Spacer	Si_{0.6}Ge_{0.4}	i		10 nm
Collector	Si	n-	1e16	250 nm
Subcollector	Si	n+	1e19	1.5 μm
Substrate	Si	p-	2e12	540 μm

Fig 6.1. Schematic of the SiGe PIN-HBT structure

$x=0.1$ (emitter side) to $x=0.4$ (collector side) to generate a quasi-electric field. This field is intended to accelerate electrons travelling through the base to collector, resulting in smaller base transit time and eventually higher cut-off frequency compared to a uniform Ge composition profile. The fabrication procedure of the circuit begins with the deposition of emitter metal(Cr/Au=500/2000 Å) by evaporation on the Si contact layer. This layer is used as an etch mask for subsequent emitter mesa etch. Emitter mesa is formed with two step etch: dry and wet etch. First, SF₆ and O₂-based anisotropic reactive ion etch (RIE) removes most portion of the emitter layer without undercut. Then, KOH-based selective wet etch is done to expose highly doped SiGe base layer with selectivity. This wet etch is accurately controlled to optimize the undercut for the minimization of the base access resistance and the successful formation of the following self-aligned base metal contact. Rapid thermal annealing(RTA) is done for the optimized ohmic contact of emitter metal in between two etch steps. Evaporation of the self-aligned base metal(Pt/Au=200/1300 Å) follows, and then base mesa is formed by RIE resulting in the exposure of the highly doped subcollector layer for collector contact. The base contact is also used as a p-contact for PIN photodiodes. Collector metal(Ti/Au=500/2000 Å) contact, also used as a n-contact for photodiode, is defined by evaporation on the exposed highly doped subcollector layer, and another RTA is performed for base and collector ohmic contact. A deep RIE is done to completely remove the subcollector layer between active devices for isolation, and SiO₂ layer(1μm) is deposited by PECVD for the separation of electrode metal contacts of the devices from following interconnection metal layer. This SiO₂ layer also behaves as a passivation layer for HBTs and an anti-reflection coating for photodiodes. Via holes for contacts are formed by selective dry etching of the SiO₂ layer, followed by the evaporation of thin film resistor (NiCr=700 Å). The measured sheet resistance of the resistors was around 25 Ω/□. Thick interconnection metal(Ti/Al/Ti/Au=500/11000/500/3000 Å) deposition is followed for the formation of measurement probing pads. Finally, airbridges are formed for the formation of inductor feedlines and crossovers of metal layers by the evaporation of thick metal(Ti/Al/Ti/Au=500/14000/500/3000 Å).

6.3 Results and Discussion

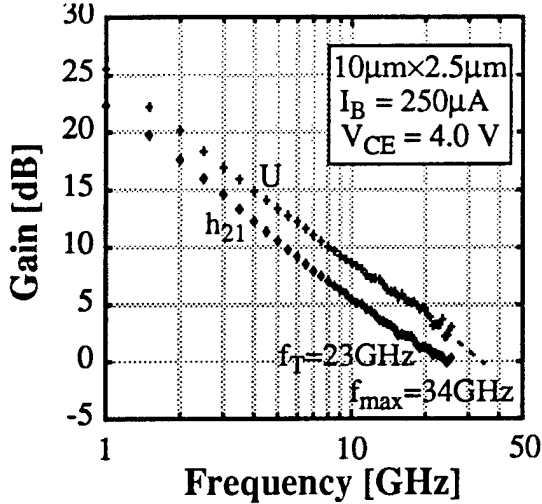


Fig. 6.2. Frequency response of the fabricated SiGe/Si HBT

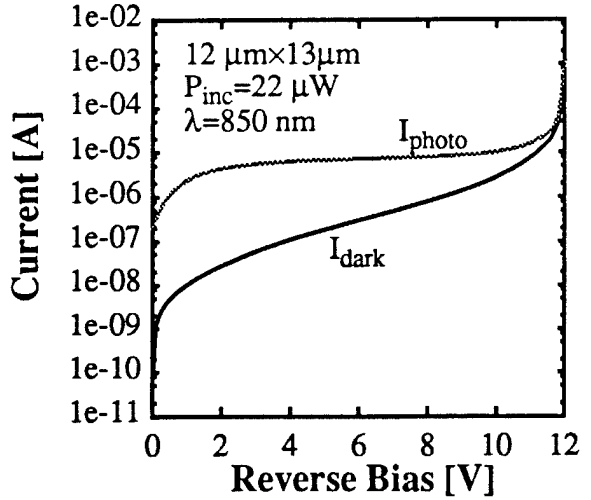


Fig. 6.3. Dark- and photo-current of the fabricated photodiode

The process described above leads to devices with high yield and excellent characteristics. From the current-voltage characteristics of HBTs with the emitter size of $2.5 \mu\text{m} \times 10 \mu\text{m}$, DC current gain β is measured to be 25 and the breakdown voltage to be 5 V. The collector and base ideality factors of the devices, extracted from its Gummel plot, are $n_c=1.12$ and $n_b=1.84$, respectively. The S-parameters were measured with a HP8510 network analyzer in the 0.5 GHz-25.5 GHz frequency range. Cut-off frequency f_T and maximum oscillation frequency f_{\max} of the device were obtained from the extrapolation of the values of current gain h_{21} and unilateral power gain U at 20 GHz with the assumption of -6 dB/octave roll-off. They are 23 GHz and 34 GHz, respectively, as shown in Fig. 6.2. The f_{\max} value is believed to be limited by the base resistance, especially base access resistance and base spreading resistance arising from the thin base region(300 Å) and insufficiently high base doping level, which is measured to be $1 \times 10^{19} \text{ cm}^{-3}$ by spreading resistance analysis. With a higher base doping level and the modification of emitter area and shape, enhanced f_{\max} value is expected.

Electrical and optical properties of mesa type PIN photodiodes, employing SiGe p+ base layer and Si n- collector layer of HBTs as p-type contact layer and intrinsic absorption layer, respectively, were characterized. The device has a $12 \mu\text{m} \times 13 \mu\text{m}$ lateral dimension and ring-shaped p-type contact, so that the incident light can be absorbed through the inner square of the ring, while the electric field in the absorption region is kept symmetric for the uniform collection of the generated carriers. Figure 6.3 shows the dark- and photo-current of a device with the incident light of power $P_{\text{inc}}=22 \mu\text{W}$ at $\lambda=850 \text{ nm}$. The dark-current level of the photodiodes were measured to be 100-200 nA at 5 V, which is rather high. The high values are believed to result from the base metal annealing during which base metal possibly penetrates through the thin base layer, leaving the B-C junction leaky. The measured responsivity has a typical value of 0.3 A/W at 5 V and increases steadily as the reverse bias is increased. This responsivity is quite reasonable for optical receiver applications. Corresponding external quantum efficiency is 43%. The bandwidth of the photodiodes was measured with the following measurement setup. Light from a GaAs semiconductor laser with the center frequency of $\lambda=850 \text{ nm}$ was coupled into a single-mode optical fiber and modulated by an modulator and a HP8350 sweeper. A polarization controller was inserted at the

input of the modulator to minimize the coupling loss. The modulated light was focused on photodiodes with a tapered optical probe and the electrical response of devices was measured with a HP8593A spectrum analyzer. An amplifier was inserted at the input of the spectrum analyzer to enhance the power level of the electrical response of photodiodes. The bandwidth of the photodiodes measured were around 450 MHz at the reverse bias of 9 V. It was observed that the bandwidth increases as the applied reverse bias increases. This relatively low bandwidth can be ascribed to the slow diffusion effect of the generated carriers. The intrinsic absorption region of the fabricated photodiodes was proved to be too thin and only a small portion of the incident photons are absorbed in that region. A much more numbers of photons are absorbed and corresponding carriers are generated in subcollector and bulk regions, in which case the photo-generated carriers travel a long distance to reach electrodes by slow diffusion mechanism, resulting in a small bandwidth. By a simple calculation, we can obtain the ratio of photon absorption in the intrinsic region to the total photon absorption. The total photocurrent consists of drift(J_{drift}) and diffusion($J_{diffusion}$) components, which arise from the carrier generation in the depleted region and the neutral region, or intrinsic region and subcollector/bulk region in the given structure, respectively. Each component can be expressed in terms of the device parameters as[24],

$$J_{drift} = -q \int_0^W G(x)dx = q\Phi_0(1 - e^{-\alpha W}) \quad (1)$$

$$J_{diffusion} = q\Phi_0 \frac{\alpha L_p}{1 + \alpha L_p} e^{-\alpha W}, \quad (2)$$

where $G(x)$ is the hole-electron pair generation rate, Φ_0 is the incident photon flux per unit area, α is the absorption coefficient, W is the width of the intrinsic region, and L_p is the hole diffusion length in the bulk region. Therefore, the ratio of the number of the generated of carriers in the intrinsic region to the total number of the generated of carriers, which is identical to the ratio of photon absorption in the intrinsic region to the total photon absorption, can be expressed as,

$$\frac{J_{drift}}{J_{total}} = \frac{J_{drift}}{J_{drift} + J_{diffusion}} = \frac{(1 + \alpha L_p)(1 - e^{-\alpha W})}{(1 + \alpha L_p - e^{-\alpha W})}. \quad (3)$$

By substituting $\alpha=650 \text{ cm}^{-1}$ for Si at $\lambda=850 \text{ nm}$, $W=250 \text{ nm}$, $L_p=4.5 \mu\text{m}$ in the subcollector, we obtain the value of the ratio to be 0.068. This implies that less than 7% of the total carrier generation occurs in intrinsic region, while more than 93% of the total carrier generation occurs either in subcollector or bulk region in the given photodiode structure. This strongly suggests that the bandwidth of the device is dominated by the carriers generated in the subcollector and bulk region which is very slow, and this explains the measured small bandwidth. By increasing the thickness of the intrinsic layer, more portion of the injected photons are expected to be absorbed in the intrinsic layer so that transit time through the depletion layer dominates the speed of the device, leading to the improvement of bandwidth. This is contrary to the common belief that the thinner the intrinsic layer, the larger the bandwidth. Too thick an intrinsic layer, however, will result in the increase of transit time, leading to the degradation of the speed. This implies that there exists an optimum value for the intrinsic layer thickness in terms of the bandwidth of photodiodes.

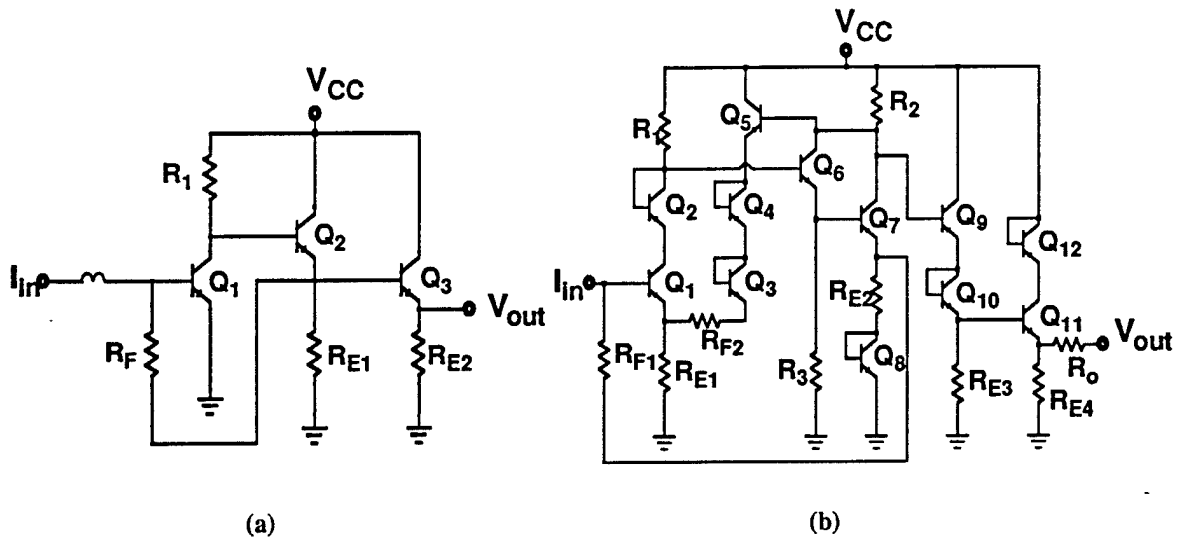


Fig. 6.4. (a) Circuit diagram of the fabricated single-feedback transimpedance amplifier
 (b) Circuit diagram of the fabricated dual-feedback transimpedance amplifier

Single- and dual-feedback transimpedance amplifiers based on SiGe/Si HBTs with emitter size of $5\mu\text{m} \times 5\mu\text{m}$ were designed, fabricated and characterized. Figure 6.4(a) shows the circuit diagram of the single-feedback transimpedance amplifier. It is composed of a common emitter gain stage, two emitter follower buffers, a resistive feedback loop, and a front-end inductor. The feedback resistor R_F determines the bandwidth, gain, and noise characteristics of the amplifier and the value should be selected based on the trade-off between these parameters. By the increase of R_F value, the gain and noise characteristics of the amplifiers are improved, while the bandwidth is degraded. In this study, the value of R_F was chosen to be $550\ \Omega$, with slightly more emphasis on the bandwidth. The circuit diagram of the dual-feedback amplifier is shown in Fig. 6.4(b). It includes a second gain stage following the first one, and an extra feedback loop including a resistor R_{F2} . This second feedback, along with the reduced value of R_{F1} ($200\ \Omega$), increases the bandwidth of the amplifier. Second gain stage amplifies the signal to a higher level, compensating for the possible reduction of gain at the first stage from the additional feedback resistance, consequently leading to an increase in overall gain-bandwidth product of the amplifier compared to the single-feedback amplifier. The S-parameters of the fabricated amplifiers were measured with a HP8510 network analyzer in the $0.1\ \text{GHz}$ - $10.0\ \text{GHz}$ frequency range. Figure 6.5(a) shows the transimpedance gain versus frequency characteristics of a single-feedback amplifier circuit. It shows a transimpedance gain of $45.2\ \text{dB}\Omega$ and $-3\ \text{dB}$ bandwidth of $3.2\ \text{GHz}$ at the bias point $V_{CC}=3\ \text{V}$. The frequency response of a dual-feedback amplifier is shown in Fig. 6.5(b). The transimpedance gain is $47.4\ \text{dB}\Omega$ and the $-3\ \text{dB}$ bandwidth is measured to be $3.3\ \text{GHz}$ at the bias point of $V_{CC}=7\ \text{V}$, which shows improvement in both gain and bandwidth compared with the single-feedback version as the design of the circuit intended. Some uncharacteristic ripples are shown in the frequency response of the amplifiers. These are believed to originate from an electrical oscillation generated within the measurement system consisting of the network analyzer and a DC voltage power supply. A moderate gain overshoot can also be seen in the frequency response of the circuits. This is ascribed to the parasitic inductance arising from the narrow coplanar ground line

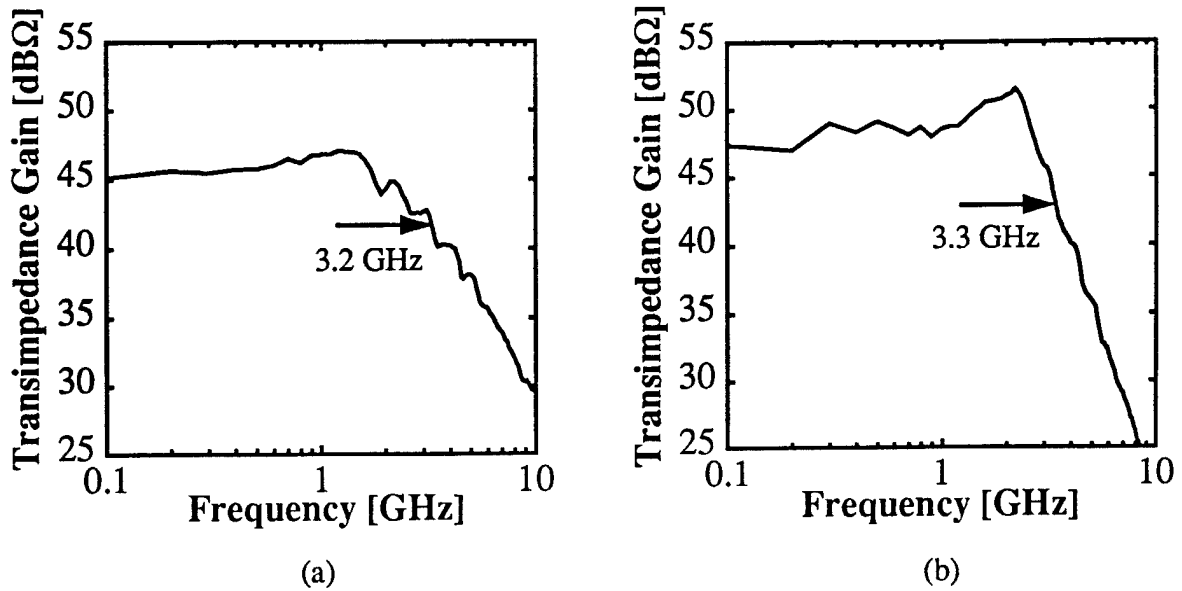


Fig. 6.5. (a) Frequency response of the fabricated single-feedback transimpedance amplifier

surrounding the whole circuit.

Monolithically integrated photoreceivers based on SiGe/Si HBTs and PIN photodiodes were designed, fabricated and characterized. Figure 6.6 shows the circuit diagram of the single-feedback photoreceiver. The topology is basically same as the single-feedback transimpedance amplifier described above, except for the diodes on each stage employed in order to optimize the bias points. The feedback resistance R_F has the value of 400Ω . The frequency response of the photoreceiver was measured with the identical measurement setup for the photodiodes described above. The relative response of the photoreceiver with the bias point of $V_{CC}=6$ V for the amplifier circuit and $V_{DD}=9$ V for the photodiode is shown in Fig. 6.7. The -3 dB bandwidth is measured as 460 MHz, which is much smaller than that of the transimpedance amplifier with similar topology. It is obvious that the bandwidth of the photoreceiver is limited by the bandwidth of the incorporated photodiode, not by the transimpedance amplifier which is often the case. The cause of the small bandwidth of the photodiode is described above and it can be improved by the optimization of the intrinsic layer thickness. If the bandwidth of the photodiodes exceeds that of transimpedance amplifiers by structure optimization, the bandwidth of the photoreceivers will be determined by the bandwidth of the transimpedance amplifiers. The bandwidth of transimpedance amplifiers may be improved by design optimization even with the current technology, and this will lead to the increase of the bandwidth of the photoreceivers to several GHz, in which case the circuit may be applied to multi Gb/s applications. As the absorption layer of the PIN SiGe photodiode is composed of Si, the operating wavelength range of the fabricated photoreceivers will be suitable for optical data link application, which does not require $1.3 \mu\text{m}$ nor $1.55 \mu\text{m}$ wavelength for low dispersion and loss. By implementing the collector layer of the SiGe/Si HBT, which is shared as the

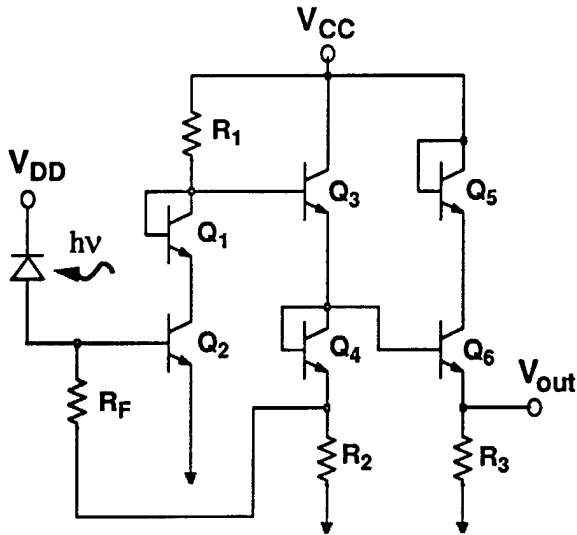


Fig. 6.6. Circuit diagram of the fabricated photoreceiver

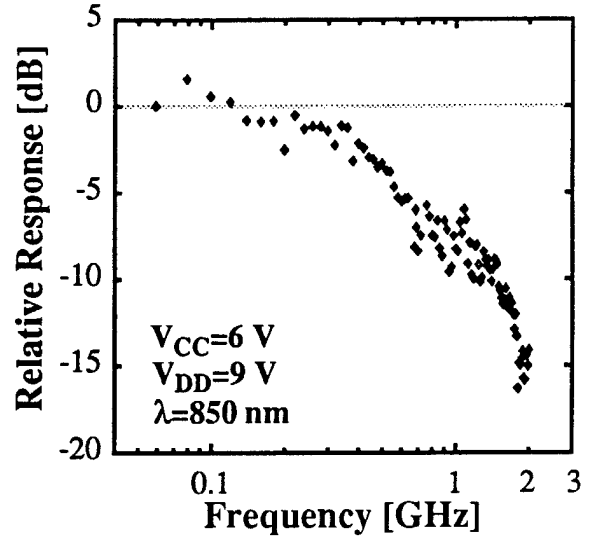


Fig. 6.7. Frequency response of the fabricated photoreceiver

absorption layer of the photodiode, with SiGe alloys with 20%-40% Ge concentration, the detectable wavelength range of the SiGe photoreceiver will be extended up to $1.3\text{ }\mu\text{m}$ and even to $1.55\text{ }\mu\text{m}$, and it may find applications even in long-haul optical communication systems. To implement the thick absorption layer with relatively high Ge concentration without significant dislocation, special buffer layers such as graded SiGe buffer layers, superlattice buffer layers, or low temperature Si buffer layers will be required[25].

6.4 Conclusion

SiGe/Si PIN-HBT technology has been developed and applied to the fabrication of transimpedance amplifiers and monolithic SiGe/Si photoreceivers for the first time. A SiGe/Si HBT exhibited the f_T and f_{max} of 23 GHz and 34 GHz, respectively, with the DC gain of 25. Mesa-type PIN photodiode showed responsivity of 0.3 A/W at $\lambda=850\text{ nm}$ and diffusion limited bandwidth of 450 MHz. Fabricated single- and dual-feedback transimpedance amplifiers exhibited the bandwidth of 3.2 GHz and 3.3 GHz with the transimpedance gain of $45.2\text{ dB}\Omega$ and $47.4\text{ dB}\Omega$, respectively. Fabricated monolithic photoreceiver showed the bandwidth of 460 MHz, which is apparently limited by the performance of photodiodes. With the optimization of the PIN-HBT material structure, the bandwidth of the photodiode is expected to be improved to exceed that of transimpedance amplifiers. Combined with the design optimization of the transimpedance amplifiers, this will result in monolithic SiGe/Si photoreceivers operating at multi Gb/s for optical communication applications. The application can be extended to long-haul fiber optical communication systems by employing SiGe alloy to the absorption layer of PIN photodiode.

7. Electro-Absorption and Electro-Optic Effect in SiGe/Si Quantum wells: Realization of Low-Voltage Optical Modulators

7.1 Introduction

The realization of optoelectronic and optical devices with SiGe/Si heterostructures has been of interest for the possibility of integration with Si-based microelectronics [26]. While detectors and photoreceivers have been demonstrated with this heterostructure, the realization of light emitters and modulators has been more elusive. Light modulators are of particular interest for silicon-based optoelectronics and optical interconnects.

Quantum-well modulators based on the Stark effect, commonly known as quantum-confined stark effect (QCSE) modulators [27], have been very successful with III-V-based quantum wells. The operation of similar devices made with pseudomorphic SiGe/Si quantum wells have been largely unsuccessful [28-30]. The reason for this has become clear from the recent study by Miyake et al. [31], and originates from the small conduction band offset, ΔE_c , of SiGe/Si heterostructure [32]. The electron wavefunction is very weakly localized in the conduction band well even under flat-band (zero-field) conditions. With the application of even a small transverse electric field, the exciton binding energy is sharply reduced, leading to a blue shift of the transition energy. This blue shift more than balances the field induced red shift due to the Stark effect. As a result, the QCSE is not observed in SiGe/Si modulators [31]. It might be possible to make modulators with SiGe/Si type-II quantum wells because of the very large electron effective mass ($0.92 m_0$) and consequently large exciton binding energy in these structures [28]. However, such devices are yet to be realized.

Interestingly, however, the weak confinement of the electron wavefunction in the SiGe/Si type I quantum well can be utilized to realize a low-voltage modulator. It may be noted that the Si and Ge lattices are centro-symmetric and therefore exhibit no electro-optic effect. In SiGe/Si quantum wells, photons with energy equal to the electron-heavy hole transition energy will be absorbed with phonon participation under flat-band conditions. A small transverse electric field will reduce the oscillator strength of this transition due to delocalization of the electron wavefunction (while the heavy hole remains confined) and the absorption will be reduced to small value. Thus, modulation will be dependent on controlling the overlap integral between the electron and hole wavefunctions. It is important to note that unlike the QCSE electroabsorption modulator, the photon energy of choice in this scheme, for optimal operation, should be higher than the bandgap of the SiGe well.

Because $Si_{1-x}Ge_x$ remains an indirect bandgap semiconductor for all values of x , most of the absorption-related work has focussed on inter-subband absorption [33-38]. To our knowledge, there has been no theoretical or experimental study of interband absorption phenomena in SiGe/Si quantum wells. The objective of the present study was therefore to explore the dependence of the absorption coefficient of SiGe/Si quantum wells as a function of transverse bias both theoretically and experimentally. We have examined both symmetric (square) and asymmetric (graded gap and coupled) quantum wells. To complete the study, the refractive index change and the corresponding

electro-optic coefficient have also been determined.

7.2 Theoretical Techniques

7.2.1 Envelop Function

The electronic properties of the heterostructures are obtained by solving Schrödinger's wave equation and Poisson's equation. The carrier wavefunctions are evaluated using the time-independent Schrödinger equations

$$\left[\frac{-\hbar^2}{2m_n} \cdot \frac{d}{dz} + V_n(z) \right] \psi^n(z) = E_i \psi^n(z) \quad (1)$$

$$\left[\frac{-\hbar^2}{2m_p} \cdot \frac{d}{dz} + V_p(z) \right] \psi^p(z) = E_j \psi^p(z) \quad (2)$$

where $V_n(z)$, $V_p(z)$ represent the electron and the hole confining potentials, respectively, m_n , m_p are the effective mass of the electron and the hole, respectively, $\psi^n(z)$, $\psi^p(z)$ are the envelope functions of the electron and the hole, respectively, E_i , E_j are the energy eigenvalue of the electron and the hole, respectively, z is the growth direction, and \hbar is the normalized Planck constant.

The electrostatic potential of the electrons in the intrinsic region, $V_n(z)$, can be written as:

$$V_n(z) = V_e(z) + qFz \quad (3)$$

where q is the electronic charge, F is the electric field, and $V_e(z)$ is potential step function due to the band discontinuity at the heterointerface. A similar electrostatic potential of the holes is assumed.

7.2.2 Absorption Coefficient and Refractive Index

From the Fermi Golden rule, the transition probability between the i and j states for indirect-band gap material quantum well can be written as:

$$W_{ij} = \frac{q^2 A^2 \pi J_v |a \cdot p_{if}|^2 M_q^2}{\hbar^2 m_o^2 L_w^2 (E_{gd} - \hbar\omega)^2} \int_0^{E_m^{ij}} N_{2v}(E) N_{2c}(E_m^{ij} - E) dE \quad (4)$$

The absorption coefficient can be evaluated from the transition probability using the relation

$$\alpha_{ij} = \frac{2\hbar W_{ij}}{\omega n_r A^2 \epsilon_o c}$$

The absorption coefficient is rewritten as:

$$\alpha_{ij} = \frac{2q^2 \pi J_v |a \cdot p_{if}|^2 M_q^2}{\omega n_r \epsilon_o c m_o^2 L_w^2 (E_{gd} - \hbar\omega)^2} \int_0^{E_m^{ij}} N_{2v}(E) N_{2c}(E_m^{ij} - E) dE \quad (5)$$

where L_w is the width of the quantum well, J_v is the number of minima in the conduction

band, A is the vector potential, c is the speed of light, $\hbar\omega$ is the photon energy, $N_{2v}(E)$ and $N_{2c}(E)$ are the two dimensional density of states in the valence and conduction bands respectively, E_{gd} is the direct band gap, M_q^2 is the matrix element for phonon scattering, a is the polarization vector of the radiation, p_{if} is the momentum matrix element, and E_m^{ij} is given by:

$$E_m = \hbar\omega \pm (\hbar\omega_p - E_{gin} - E_i - E_j)$$

Here \pm is for phonon absorption and emission, $\hbar\omega_p$ is the phonon energy, and E_{gin} is the indirect band gap.

The imaginary part of the dielectric constant is given in term of the absorption coefficient as:

$$\epsilon_I = \frac{n_r c \alpha}{\omega}$$

The real part of the dielectric constant depends on the frequency of the electromagnetic wave and is related to the imaginary part of the dielectric constant by the Kramers-Krönig relation

$$\epsilon_R = 1 + \frac{2}{\pi} \cdot P \int_0^\infty \frac{\eta \epsilon_I(\eta)}{\eta^2 - (\hbar\omega)^2} d\eta \quad (6)$$

where η denotes the photon energy, and P is the principle value of the integral. The refractive index is evaluated using the relation

$$n_r^2(\omega) = \left[\frac{\epsilon_R + \sqrt{\epsilon_R^2 + \epsilon_R^2}}{2} \right] \quad (7)$$

The change in the refractive index can be modeled in terms of the applied voltage as:

$$\Delta \left(\frac{1}{n_r^2} \right) = rF + sF^2 \quad (8)$$

where r and s are the linear and quadratic electrooptic coefficients, respectively. In evaluating the refractive index in the quantum well we assume that the absorption coefficient due to the two dimensional quantum well remains constant in the continuum state with increasing photon energy (i.e for $\hbar\omega$ greater than the bandgap of Si).

7.2.3 Results and Discussion

The calculated optical properties of $\text{Si}_{1-x}\text{Ge}_x/\text{Si}$ type-I quantum well structures are presented in this section. The parameters used in the calculation are $x=0.4$, $\Delta E_c=0.02$ eV, $\Delta E_v=0.296$ eV, and the other parameters are taken from Ref. 14. The simulation is performed on square quantum well (SQW), coupled quantum well (CQW), and graded quantum well (GQW) structures. The energy band diagrams for these structures are shown in Fig. 7.1. The quantum well region is cladded by undoped (intrinsic) regions, followed by heavily doped regions, as in a conventional electroabsorption modulator. The modulator can also be a Schottky barrier diode with a top metal contact on the n-type barrier material, with the quantum well region being undoped.

To optimize the performance of the modulators, an accurate knowledge of the quantum well parameters is required. From the Fermi Golden rule, the absorption coefficient is found to be

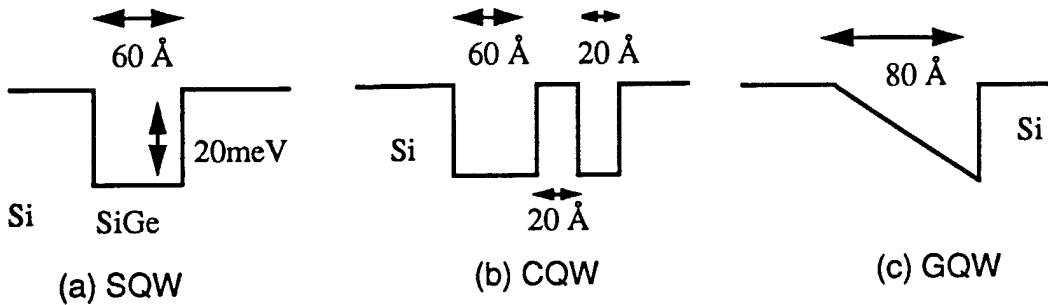


Figure 7.1: Energy band diagram for (a) square quantum well (SQW), (b) coupled quantum well (CQW), and (c) graded quantum well (GQW).

inversely proportional to the square of the quantum well width. This dependence suggests using a narrow quantum well. In fact, decreasing the well width will increase the transition energy. Moreover, the overlap integral between the electron and the hole wavefunction is also function of the width of the quantum well. An optimization of the quantum well parameters is required such that the modulator is characterized by large contrast ratio, low insertion loss, low operating voltage, and operation at or near $\lambda = 1.3\mu\text{m}$. Unfortunately, the absorption coefficient near the transition energy is very small due to the indirect nature of the bandgap. From Eq.(5), it is evident that the absorption coefficient is a linear function of E_m^{ij} for parabolic density of states. As a result, the transition probability is very small for a photon energy near the indirect band gap, E_{gin} . Because of this we expect very weak exciton transition.

The solution of the Schrödinger's wave equation and Poisson equation are performed in the entire device structure because the electron confining potential is below kT at room temperature ($\Delta E_c=20\text{ meV}$) [32]. This is done by placing the boundary conditions far away from the active region. The quantum well absorption spectra are evaluated by determining the optical matrix elements. The calculation accounts the first 100 energy levels in the conduction band well. Because the electron wavefunctions extend in space, the barrier thickness is increased to large value, 2000 Å. The simulation is performed for the three structures, SQW, CQW, and GQW. The room temperature absorption coefficients as a function of photon energy are shown in Fig. 7.2 for zero electric field in the quantum well (flat-band conditions). As shown in this figure, the absorption coefficient of the SQW is the largest. The large value of α for SQW, compared with that of the CQW is due to the dependence of α on the well width. In fact, changing the well width can change the transition energy and causes a shift in the absorption spectrum. The effect of the well width on the absorption coefficient, evaluated for 1.2 μm photon wavelength and zero electric field, is shown in Fig. 7.3 for a SQW. As can be seen, the absorption coefficient peaks for $L_w=35\text{\AA}$. This is mainly due to a shift in the absorption spectrum as the well width decreases.

Because the valence band discontinuity between $\text{Si}_{1-x}\text{Ge}_x$ and Si is large ($\Delta E_v=0.74x\text{ eV}$) [32], the hole wavefunctions are almost localized in the quantum well. On the other hand, the conduction band discontinuity is only 20 meV [32]. As stated earlier, these characteristics can be utilized to realize a low voltage electroabsorption modulator/switch. The modulation mechanism can be described as follows: The electron wavefunction is localized in the shallow quantum well under zero electric field (flat-band condition). Under these conditions, the overlap integral between the electron and the hole wavefunction is large. As the bands are bent with applied bias, the electron

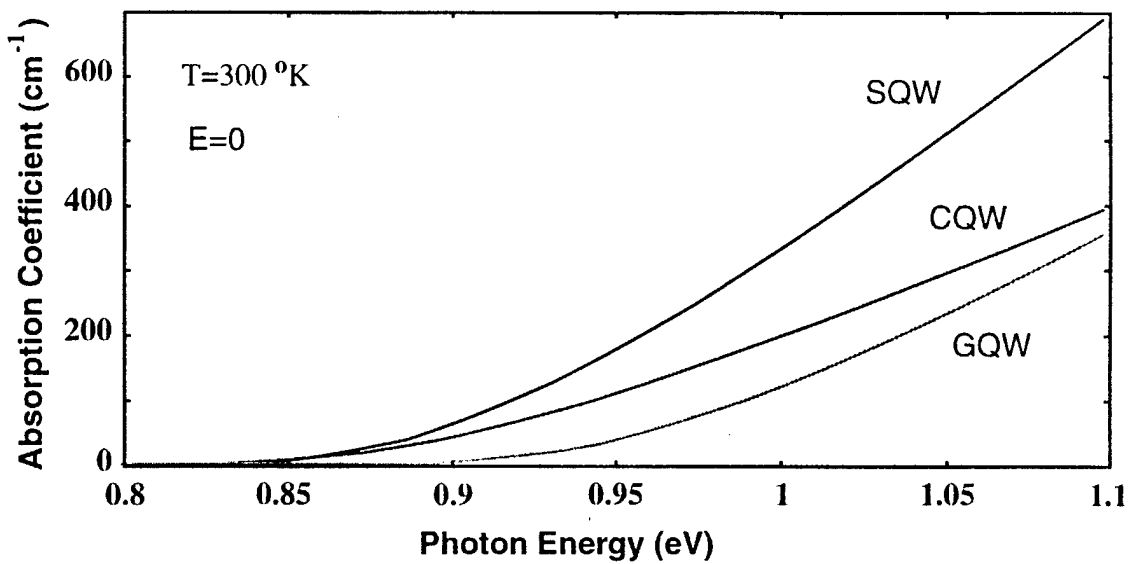


Figure 7.2: Absorption coefficient as a function of photon energy at zero transverse field for SQW, CQW, and GQW structures.

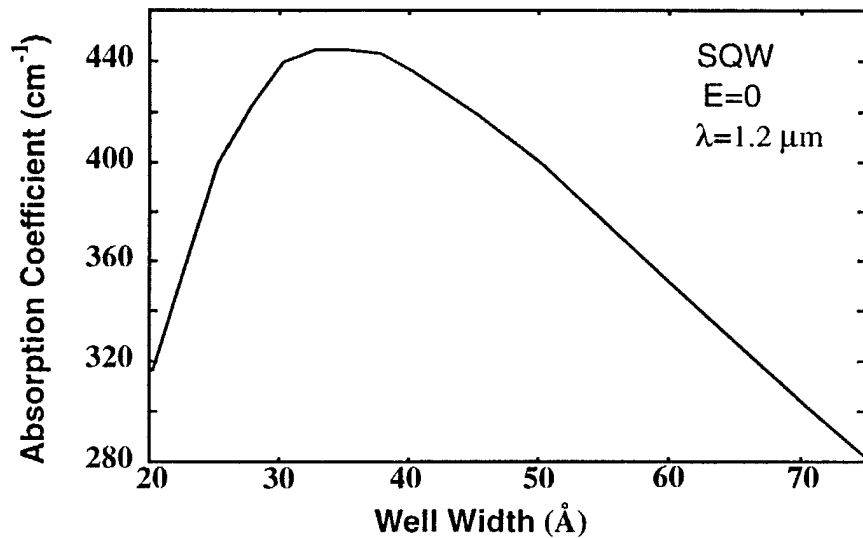


Figure 7.3: Absorption coefficient as a function of well width for a SQW at zero transverse field.

wavefunction moves out of the well region [31]. This reduces the overlap integral between the electron and the hole. As a result the absorption coefficient decreases to a small value with a small change in the electric field.

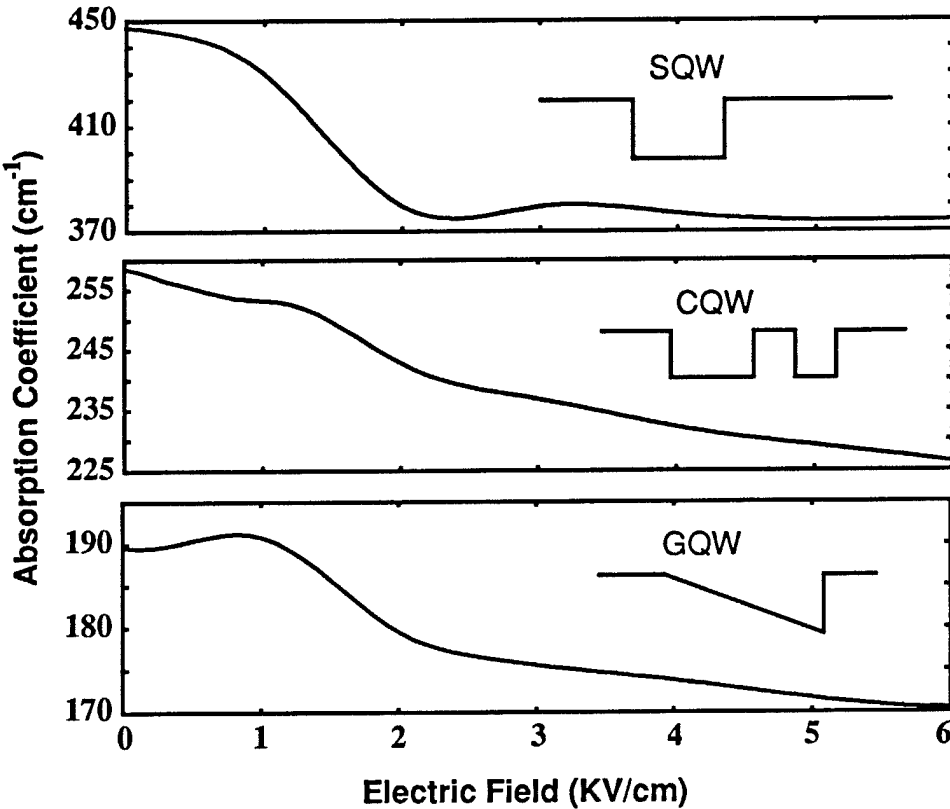


Figure 7.4: Absorption coefficient as a function of transverse field for (a) SQW, (b) CQW, and (c) GQW structures.

The shape and the size of the quantum well has a considerable impact on the overlap integral. As shown in the calculated results of Fig. 7.4, the largest change in the absorption coefficient between the on and off-states is obtained for the SQW for a small change in the electric field. It is important to note that although the absorption coefficients are small, as expected, due to the indirect nature of the materials involved, the modulation action is made very efficient by the manner in which the absorption is turned off. Furthermore, the device speed can also benefit from the small conduction band offset where the electrons can sweep out of the quantum well and result in a fast switching speed [40].

The large change in the absorption coefficient for the SQW is associated with a large change in the refractive index, as shown in Fig. 7.5. This change can be utilized to design electro-optic phase modulators. The values of the linear and quadratic electrooptic coefficient, obtained by fitting the data of Fig. 7.5 with Eq. (8), are given in Table I.

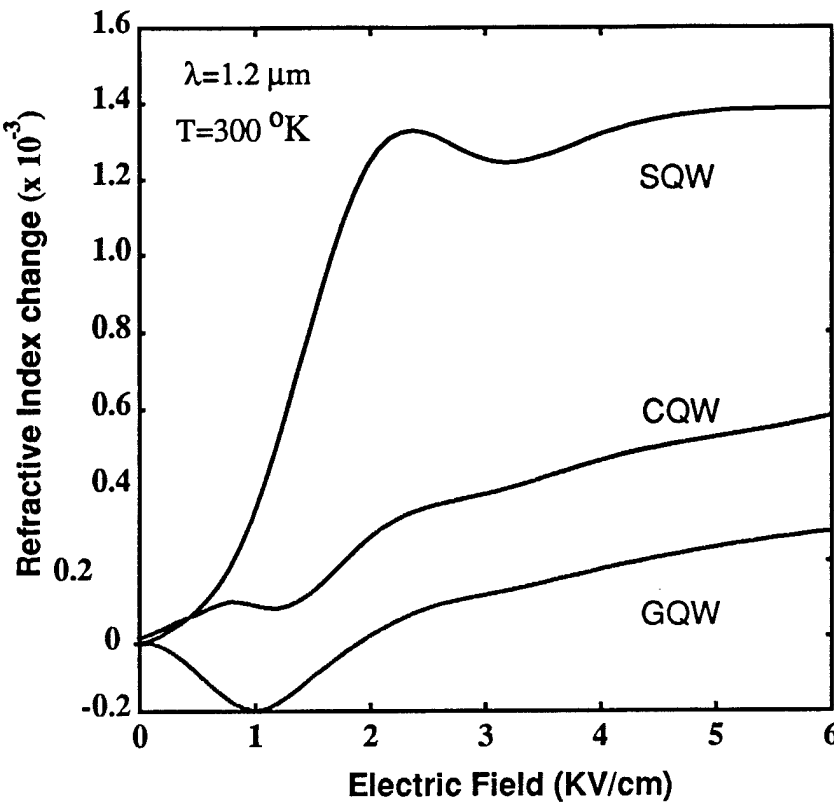


Figure 7.5: Refractive index changes as a function of transverse field for SQW, CQW, and GQW structures.

Table 1: Calculated values of the electrooptic coefficients

Quantum Well Type	r (m/V)	s (m ² /V ²)
SQW	1.9×10^{-10}	1.9×10^{-16}
CQW	2.4×10^{-11}	1.0×10^{-16}
GQW	3.8×10^{-11}	2.0×10^{-17}

It is evident that efficient amplitude or phase modulation can be achieved with the use of square SiGe/Si quantum wells in an appropriate device configuration. The photon energy will have to be coincident with the electron-heavy-hole transition energy and it appears that the devices can be designed near 1.3 μm incident light. In the case of QCSE modulators made with III-V materials, a multiquantum well (MQW) active region is generally used to increase the

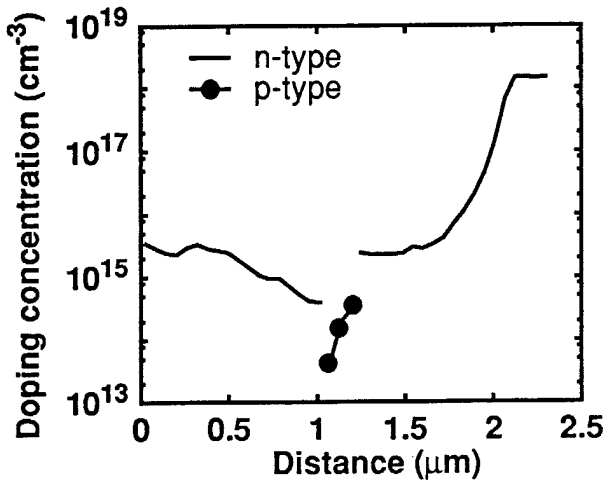
absorption of the incident light. Because the electron and hole wavefunctions are localized in the individual wells up to fairly high ($\approx 10^5$ V/cm) values of transverse electric field, the absorption behavior remains almost identical in each well. In the case of the SiGe/Si MQW, this is not true since the electron wavefunction in each well is very weakly confined. Therefore, the absorption is very much dependent on the barrier thickness and a unique average behavior is obtained for each MQW configuration. We believe that the best modulator design will consist of multiple wells spaced by 2000-3000 Å barriers so that the absorption behavior of all the wells remain identical. These wells are placed in an undoped Si layer. A transverse field can be applied either with heavily doped n regions or by a Schottky contact. In the latter case, the wells are placed outside the depletion region at zero bias. The device itself will have a guided wave geometry.

7.3 Experimental Study

The desired $\text{Si}_{0.6}\text{Ge}_{0.4}/\text{Si}$ waveguide heterostructure, grown by MBE on n^+ (001) Si substrate, is shown in Fig. 7.6(a). The single-mode guiding region consists of three periods of 40 Å SiGe wells and 1000 Å Si barriers, and an addition 250 Å $\text{Si}_{0.6}\text{Ge}_{0.4}$ layer. The large barrier thicknesses are used in order to ensure that the absorption behavior of all the wells are identical, in view of the very weak localization of the electron wavefunction in each well. Coupling of the wells would obscure the modulation mechanism. Thick ($\approx 1\mu\text{m}$) undoped Si cladding layers are placed on both sides of the guiding region. The upper cladding layer also ensures that the depletion region of the Schottky diode formed on top does not penetrate into the guiding region, and therefore flat-band conditions can be maintained in this region in the absence of an applied reverse bias. A 3 μm wide ridge waveguide is defined by photolithography and reactive ion etching. A Pt/Au (500/1500) Å Schottky contact is evaporated selectively on top of the ridge and a Ti/Pt/Au (500/500/2500) Å

n^- Si	$5 \times 10^{15} \text{ cm}^{-3}$	1 μm
n^- $\text{Si}_{0.6}\text{Ge}_{0.4}$	40 Å	
n^- Si	1000 Å	} x 3
n^- $\text{Si}_{0.6}\text{Ge}_{0.4}$	250 Å	
n^- Si	$5 \times 10^{15} \text{ cm}^{-3}$	0.7 μm
n^+ Si	$5 \times 10^{18} \text{ cm}^{-3}$	

(a)



(b)

Figure 7.6: (a) Design of ideal heterostructure for SiGe/Si quantum well modulator, and (b) doping profile of heterostructure grown by Molecular beam epitaxy as measured by SRA.

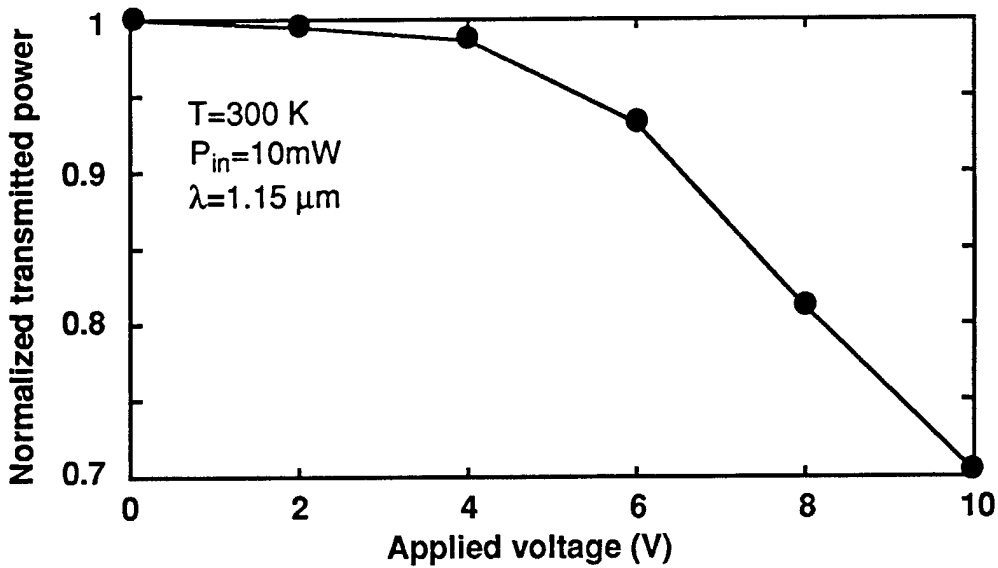


Figure 7.7: Measured transmission as a function of applied bias in a $100 \mu\text{m}$ long device.

ohmic contact is formed on the top surface of the substrate. A $0.8\mu\text{m}$ SiO_2 passivating layer is deposited by PECVD and the interconnection metals are evaporated thereafter. The substrate is then thinned to $90\mu\text{m}$ and $100\mu\text{m}$ long waveguides are delineated by scribing and cleaving. The Schottky diodes have leakage currents $\approx 2 \mu\text{A}$ and reverse breakdown voltage of 32V .

Assuming flat-band conditions in the quantum wells with zero applied bias to the Schottky diode - a condition that would normally be achieved for n-doped barrier and guiding layers - the absorption coefficient would be reduced to a small value with only a transverse applied field of $2\text{KV}/\text{cm}$. The actual doping profile in the heterostructure, as measured by spreading resistance analysis (SRA), is shown in Fig. 7.6(b). In fact, the quantum well region is unintentionally doped p-type and as a result a p-n junction field is created across the quantum wells, whose value is estimated to be $3.5\text{KV}/\text{cm}$. Because of this field, the electron wavefunctions are initially delocalized with no applied bias to the Schottky diode and the absorption coefficient is expected to have a small value. Because the electric field in the n-p-n structure is not uniform, a positive bias will be required to create flat-band conditions in the well regions and increase the absorption coefficient. Therefore, as a modulator, the device is expected to have a high transmission at zero applied bias and low transmission at positive applied bias to the Schottky diode. Note that we have not realized the desired structure, but as will be evident, the modulation behavior expected from such structures is attained.

The electro-absorption properties of the device were examined by measuring the transmitted light as a function of applied bias. Light from a $1.15\mu\text{m}$ HeNe laser (10mW output power) was coupled to one end of the waveguide through an objective lens and a polarizer. The polarization of the input light was normal to the layers. The transmitted light as a function of applied bias is plotted in Fig. 7.7. The data corresponds to a modulation depth of 5.44 dB . Note that the large bias results primarily from the voltage drop across the regions outside the quantum wells. With a uniformly n-doped structure and slightly more optimized device design, this bias can be reduced substantially. As can be seen from Fig. 7.7, the transmission does not saturate at high applied voltage

where flat-band conditions are expected. This is mainly due to the fact that the electric field in the well regions is determined by the voltage drop across the n-p-n structure. Since the width of the lightly doped p-type region is very small, the 10V applied voltage is not enough to achieve flat-band conditions in the well regions. The voltage drop across the n-p-n structure at 10V applied voltage is only 0.23V, calculated with the Mott-Gurney law [41]. The measured change in the absorption coefficient ($\Gamma\Delta\alpha$) as a function of the current density is shown in Fig. 7.8, where Γ is the optical confinement factor. The change in the absorption coefficient of the device is as high as 34 cm^{-1} at 10V applied voltage. It is important to consider the contribution of free carriers to this change in absorption coefficient. This contribution can become significant for free carrier concentrations larger than 10^{19} cm^{-3} [42] and long device lengths. For $\lambda=1.15\mu\text{m}$, the change in absorption coefficient due to free carriers is given by $\Delta\alpha_f(\text{cm}^{-1})=3.87\times10^{-19}(n+p)$ where n and p are the free electron and hole concentrations in cm^{-3} . The concentrations were calculated for 10V applied voltage to the device using the technique outlined in Ref. [43]. The corresponding value of $\Delta\alpha_f$ is derived to be $\approx 0.4\text{ cm}^{-1}$. However, the presence of free carriers will slightly enhance the modulation ratio of the device.

The change in absorption coefficient is usually accompanied by a change of refractive index near the bandgap, in accordance with the Kramers-Krönig relation, leading to an electro-optic phase retardation of the transmitted light. Because our devices are only $100\mu\text{m}$ long, no observable phase retardation of light, launched at 45° to the diode electric field with an input polarizer, was noted with an output analyzer. Experiments with longer devices are planned.

It should be noted that in order to observe amplitude modulation the photon energy of the incident light should be slightly larger than the bandgap in the $\text{Si}_{0.6}\text{Ge}_{0.4}$ quantum wells. As a result the modulator exhibits a large insertion loss. The calculated insertion loss and contrast ratio, as a function of the modulator length, using square quantum wells, are shown in Fig. 7.9 for $\lambda=1.15\mu\text{m}$. It is clear that there is a trade-off between the two parameters. However, for a device length of $100\mu\text{m}$, which we have used, the contrast ratio (on/off ratio) is 2.9, which is acceptable. The performance characteristics are by no means ideal, but with better device design and MBE growth, the performance can be considerably improved. Moreover, the modulator can be made to operate at $1.3\mu\text{m}$ by an optimum design of the quantum well parameters.

7.4 Conclusion

We present theoretical and experimental investigation of the indirect band-to-band absorption coefficient and electrooptic effect in SiGe/Si quantum well optical modulators. An investigation of the impact of the quantum well shape and dimensions on the optical properties of the optical modulator is carried out. The shift of the electron wavefunction in the shallow conduction band quantum well is utilized to control the coupling between the electrons and the holes. This results in large changes in the absorption coefficient and the refractive index and a very large value of the linear electro-optic coefficient, which indicate that novel amplitude and phase modulators can be realized with this material system. The measured modulation depth of $100\mu\text{m}$ long devices is 5.44 dB.

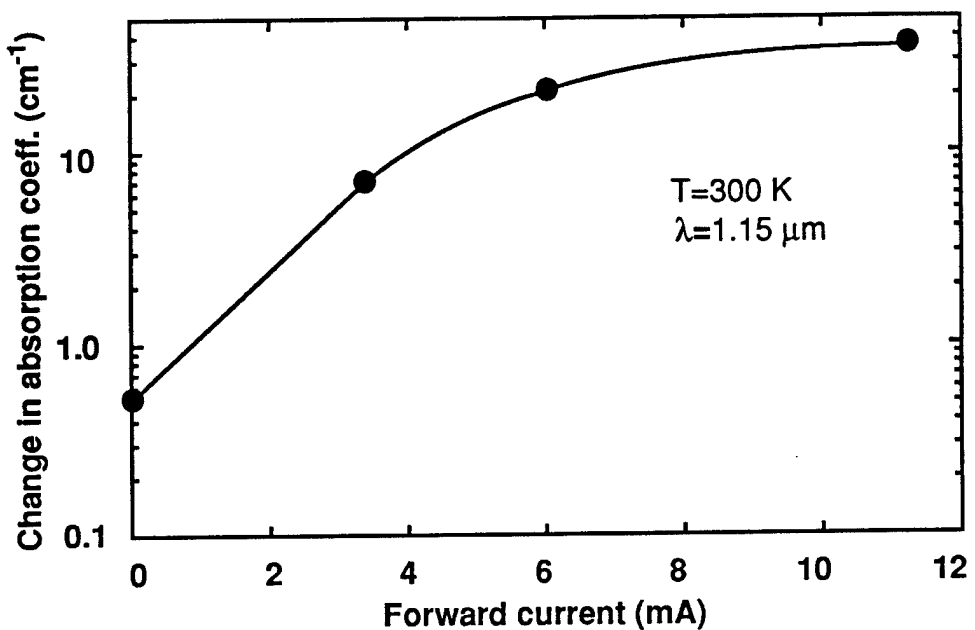


Figure 7.8: Change in absorption coefficient as a function of injected current density in 100 μm long device.

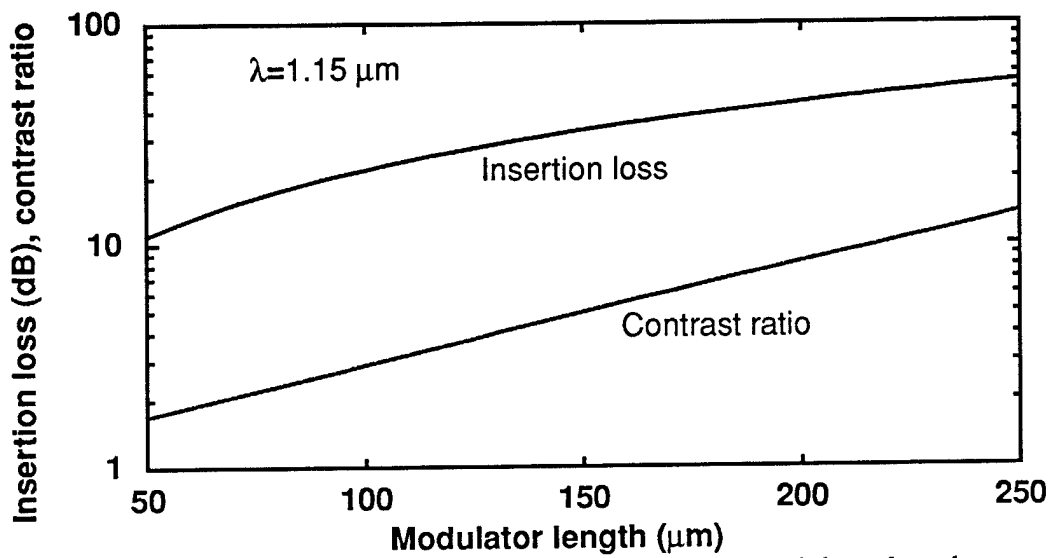


Figure 7.9: Insertion loss and contrast ratio as a function of modulator length.

8. Light Emitting Sources on Si

While III-V based components are the current materials of choice in the OEIC industry, the possibility of incorporating infrared lasers with existing Si technology has prompted the need for improving the growth conditions of III-V materials on Si substrates. Quantum dot laser technology is attractive as a component for future OEICs due to its narrow bandwidth and reduced threshold voltage. Alloying the quantum dot active region makes it suitable for the 1.3 to 1.55 μ m communications range. Room temperature lasers exploiting InAs/GaAs quantum dots on GaAs substrates have been demonstrated[44].

Fig. 8.1 shows a cross-section TEM(200) image of a InGaAs/GaAs multi-layer quantum dots grown at the University. The dots are formed by the Stranski-Krastanow method which describes island formation in response to the 7% mismatch between InAs and GaAs. Vertical alignment in the growth direction of multi-layer quantum layers is due to a strain driven self-alignment process; this process improves the size uniformity[19]. The InGaAs layers are 6-7 monolayers thick.

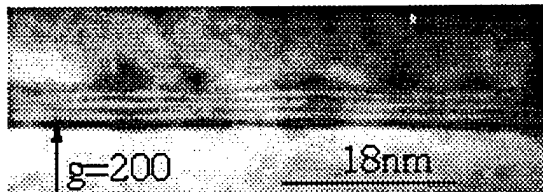


Figure 8.1. Cross-section TEM of InGaAs/GaAs multi-layer quantum dots

Growth of high quality III-V devices on Si is hindered by the formation of large defect densities because of the 4% lattice mismatch and the 250% difference in thermal expansion coefficients between GaAs and Si. InAs/GaAs quantum dot lasers would be an excellent candidate as a light emitting source for hybrid Si OEICs. The development of quantum dot lasers grown on Si substrates seems promising due to the large density of quantum dots($5 \times 10^{10} \text{ cm}^{-2}$) created during growth resulting in excellent luminescence spectrums [46]. Therefore it is critical to grow defect-free GaAs layers on Si substrates. Several authors have reported successful growth of defect-free GaAs layers on Si substrates using post-growth mesa patterning and extensive annealing procedures[47,48]. Georgakilas et al. has shown that tilting the substrate 1.5-6.0° towards the [110] direction minimizes the formation of antiphase domain boundary defects and stacking faults[49,50]. Pre-exposure of the Si substrate with As and/or Ga at low temperatures (~400°C) also reduces stacking fault defect formation[49]. The proposed structure is shown in Figure 8.2. Preliminary photoluminescence studies of InAs/GaAs QDs grown on (100) Si, shown in Figure 8.3, have been conducted, indicating a QD luminescence peak at 1.22 eV. Future studies will include growing the InAs/GaAs QD structure on (100) Si substrates titled 2° towards the [110] direction. An LT-Si buffer layer grown on the Si substrate should hinder the threading dislocation formation as well.

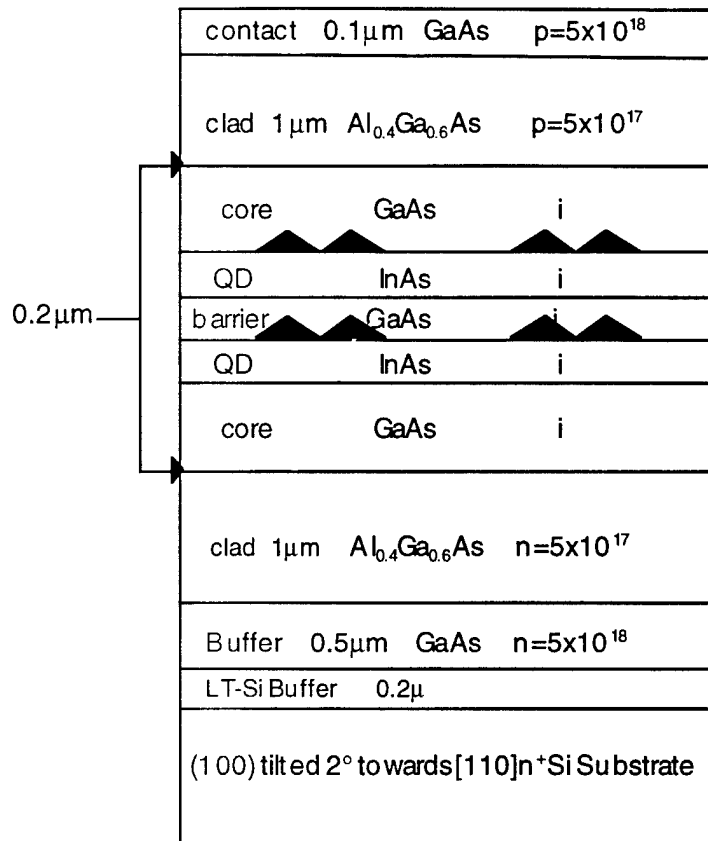


Figure 8.2. Proposed structure of InAs/GaAs quantum dot laser grown on (100) Si tilted 2° toward the [110] direction using a low temperature Si buffer.

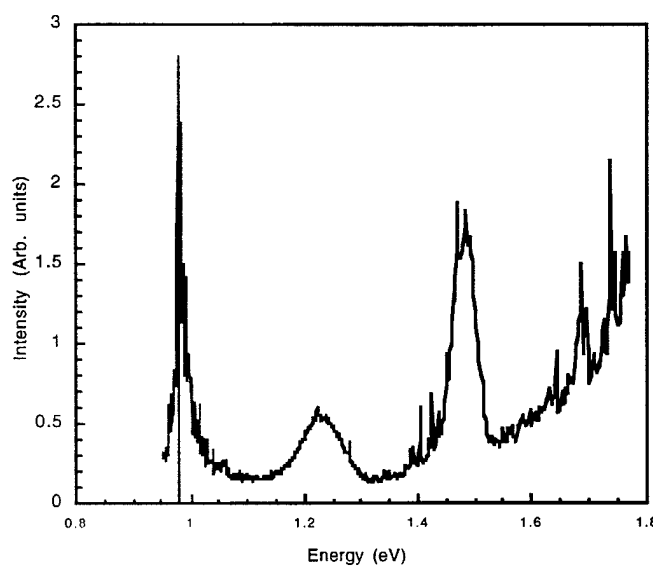


Figure 8.3. Photoluminescence measured at 77°K of InAs/GaAs quantum dots grown on (100) Si indicating the quantum dot peak at 1.22 eV.

9. Channel Effective Mass and Interfacial Effects in *p*-MOSFETs

The MOSFET technology based on Si-SiO₂ technology is the most important device technology for modern microelectronics. The p-type MOSFET (PMOS) is an integral part of this technology due to its importance in complimentary logic. In spite of the importance of the MOS there are a number of unresolved issues for both p-type and n-type devices. These include (i) Interface roughness scattering and its role in transport; (ii) Present PMOS charge models do not include the coupling of heavy-hole and light-hole bands and ignore the split-off bands; an important manifestation of the simplistic nature of the modeling of MOS physics is the significant disagreement in the calculated and measured velocity field relations.

We present results of a numerical formalism developed to address the band structure and charge control problem in p-type MOSFETs. A 6-band $k \cdot p$ Kohn-Luttinger formulation is used to describe the hole states. Our model gives the potential in a MOSFET by solving the Schrödinger equation and Poisson equation self-consistently. The Schrödinger equation yields the confined charge terms in the Poisson equation which, in turn, determines the potential profile which is fed back into the Schrödinger equation. An iterative process brings both equations into convergence simultaneously. The 6-band $k \cdot p$ Kohn-Luttinger allows us to examine the influence of the coupling of the heavy hole, light hole and the split-off bands. In addition to the charge versus gate bias relation we examine how the average in-phase hole mass depends on the sheet charge density and temperature.

As shown in Figure 9.1(a), The channel effective mass increases with sheet charge density. At low temperature, this effect is even more pronounced. Note in our model, the effective mass is calculated explicitly from the valence band structure. The hole density in the split-off band is found to be ~5% at 300K. We also study the fraction of charge near the Si-SiO₂ interface- a parameter controlling the interface scattering effect. Figure 9.1(b) shows that the probability or fraction of the ground state from the interface is not linear in the charge density. More importantly, we find that the matrix element for interface roughness scattering has significant departure from the linear model currently being used.

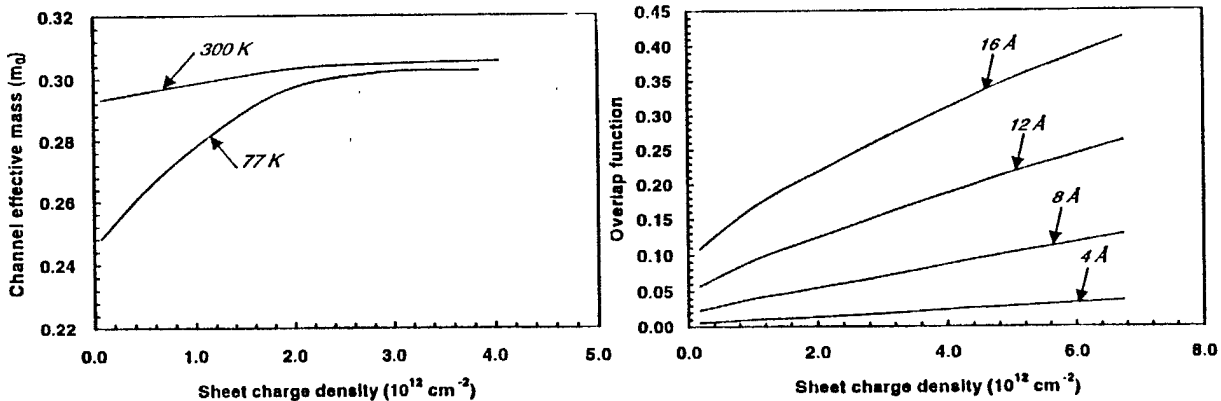


Figure 9.1 (a) In-plane hole effective mass versus sheet charge density at 300K and 77K in a PMOS. (b) The weighted overlap function of valence sub-bands versus sheet charge density at 300K.

References

- [1] R. Malik, E. Gulari, P. Bhattacharya, K. K. Linder, J. -S. Rieh, *Appl. Phys. Lett.*, **70**, 1149, (1997).
- [2] K. Ismail, F. K. LeGoues, K. L. Saenger, M. Arafa, J. O. Chu, P. M. Mooney, and B. S. Meyerson, *Phys. Rev. Lett.*, **73**, 3447, (1994).
- [3] P. M. Mooney, J. L. Jordan-Sweet, J. O. Chu and F. K. LeGoues, *Appl. Phys. Lett.*, **66**, 3642(1995).
- [4] M. A. Lutz, R. M. Feenstra, F. K. LeGoues, P. M. Mooney and J. O. Chu, *Appl. Phys. Lett.*, **66**, 724(1995).
- [5] J. H. Li, V. Holy, G. Bauer, J. F. Nützel and G. Abstreiter, *Appl. Phys. Lett.*, **67**, 789(1995).
- [6] F. K. LeGoues, B. S. Meyerson and J. F. Morar, *Phys. Rev. Lett.*, **66**, 2903(1991).
- [7] R. Hull, J. C. Bean, R. E. Leibenguth and D. J. Werder, *J. Appl. Phys.*, **65**, 4723(1989).
- [8] G. Kissinger, T. Morgenstern, G. Morgenstern and H. Richter, *Appl. Phys. Lett.*, **66**, 2083(1995).
- [9] F. K. LeGoues, *Phys. Rev. Lett.*, **72**, 876(1994).
- [10] H. Chen, L. W. Guo, Q. Cui, Q. Hu, Q. Huang and J. M. Zhou, *J. Appl. Phys.*, **79**, 1167(1996).
- [11] Amano, H., Asahi, T., and Akasaki, I., *Jap. Jour. of Appl. Phys.*, Pt. 2, **29**, L205 (1990).
- [12] J. P. Hirthe and J. Lothe, *Theory of Dislocations*, (Wiley, New York, 1982), 2nd. ed.
- [13] B. S. Meyerson, K. J. Uram and F. K. LeGoues, *Appl. Phys. Lett.*, **53**, 2555(1988).
- [14] T. Vogelsang and K. R. Hofmann, *Appl. Phys. Lett.*, **63**, 186, (1993).
- [15] J. Welser, J. L. Hoyt, and J. F. Gibbons, *IEEE Electron Device Lett.*, **15**, 100, (1994).
- [16] D. K. Nayak, K. Goto, A. Yutani, J. Murota, and Y. Shiraki, *IEEE Trans. Electron Devices*, **43**, 1709, (1996).
- [17] R. A. Soref, *Proc. IEEE*, **81**, 1687(1993).
- [18] S. Fujita, T. Sukazi, A. Matsuoka, S. Miyazaki, T. Torikai, T. Nakata and M. Shikada, *Elect. Lett.*, **26**, 175(1990).
- [19] H. Hamano, T. Yamamoto, Y. Nishizawa, Y. Oikawa, H. Kuwatsuka, A. Tahara, K. Suzuki and A. Nishimura, *Elect. Lett.*, **27**, 1602(1991).

[20] Y.S. He, L. D. Garrett, K. -H. Lee and J. C. Campbell, *Elect. Lett.*, **30**, 1887(1994).

[21] M. Yamamoto, M. Kubo and K. Nakao, *IEEE Trans. Elect. Devices*, **42**, 58(1995).

[22] M. Kyomasu, *IEEE Trans. Elect. Devices*, **42**, 1093(1995).

[23] L. D. Garrett, J. Qi, C. L. Schow and J. C. Campbell, *IEEE Trans. Elect. Devices*, **43**, 411(1996).

[24] S. M. Sze, *Physics of semiconductor devices*, 2nd Ed. New York: John Wiley & Sons, 1981.

[25] K. K. Linder, F. C . Zhang, J. -S. Rieh and P. Bhattacharya, *Appl. Phys. Lett.*, **70**, 3224(1997).

[26] D. Garrett, J. Qi, C. L.Schow and J. C. Campbell, *IEEE Trans. on Electron Devices*, **43**, 411(1996).

[27] D. A. B. Miller, D. S. Chemla, T. C. Damen, A. C. Gossard, W. Wiegmann, T. H. Wood, and C. A. Burrus, *Phys. Rev. Lett.*, **50**, 2173(1984).

[28] J. S. Park, R. P. G. Karunasiri, and K. L. Wang, *J. Vac. Sci. Technol. B*, **8**, 217(1990).

^v
[29] T. Baier, U. Mantz, K. Thonke, R. Sauer, F Schäffler and H. -J. Herzog, *Phys. Rev. B*, **50**, 15191(1994).

[30] H. Temkin, T. P. Pearsall, J. C. Bean, A. Logan and S. Luryi, *Appl. Phys. Lett.*, **48**, 963(1986).

[31] Y. Miyake, J. Y. Kim, Y. Shiraki and S. Fukatsu, *Appl. Phys. Lett.*, **68**, 2097(1996).

[32] R. People and J. C. Bean, *Appl. Phys. Lett.*, **448**, 538(1986).

[33] Y. Fu. M. Willander and W. Xu, *J. Appl. Phys.*, **76**, 3103(1996).

[34] V. D. Shadrin, V. T. Coon and F. L. Serzhenko, *Appl. Phys. Lett.*, **62**, 2679(1993).
yu

[35] F. L. Serzhenko and V. D. Shadrin, *Sov. Phys. Semicond.*, **26**, 277(1992).

[36] J. S. Park, R. P. G. Karunasiri and K. L. Wang, *Appl. Phys. Lett.*, **61**, 681(1992).

[37] C. Lee and K. L. Wang, *Appl. Phys. Lett.*, **60**, 2264(1992).

[38] K. Fujita, S. Fukatsu and Y. Shiraki, *Appl. Phys. Lett.*, **61**, 210(1992).

[39] J. Singh, *Physics of semiconductors ans their heterostructures*, New York: McGraw -Hill, 1993.

[40] J. Feldmann, K. W. Goossen, D. A. B. Miller, A. Fox, J. Cunningham and W. Jan, *Appl. Phys. Lett.*, **59**, 66(1991).

[41] A. A. Grinberg and S. Luryi, *J. Appl. Phys.*, **61**, 1181(1987).

- [42] R. A. Soref and B. R. Bennett, *IEEE J. Quantum Electron.*, **QE-23**, 123(1987).
- [43] W. Ng, S. Liang and C. T. Salama, *Solid-State Electronics*, **33**, 39(1990).
- [44] K. Kamath, N. Chervela, K. K. Linder, T. Soznowski, H. -T. Jiang, T. Norris, J. Singh, and P. Bhattacharya, submitted to *Appl. Phys. Lett.* June 1997.
- [45] J. Tersoff, C. Teichert, and T. G. Lagally, *Phys. Rev. Lett.*, **76**, 1675, (1996).
- [46] R. Apetz, L. Vescan, A. Hartmann, C. Dieker, and H. Lüth, *Appl. Phys. Lett.*, **66**, 445, (1995).
- [47] J. P. van der Ziel and N. Chand, *J. Appl. Phys.*, **68**, 2731(1990).
- [48] T. Egawa, J. Dong, K. Matsumoto, T. Jimbo and M. Umeno, *IEEE Photon. Technol. Lett.*, **7**, 1264(1995).
- [49] A. Georgakilas, Ch. Papvassiliou, G. Constantidis, K. Tsagaraki, H. Krasny, E. Löchtermann, and P. Panayotatos, *Appl. Surf. Sci.*, **102**(1996), 67.
- [50] A. Georgakilas, P. Panayotatos, J. Stoemenos, J. -L. Mourrain and A. Christou, *J. Appl. Phys.*, **71**(1992), 2679.

LIST OF PUBLICATIONS

1. "Monte Carlo Studies of Ohmic Hole Mobility in Silicon and Germanium: Examination of the Optical Phonon Deformation Potential", J.M. Hinckley and J. Singh, *J. Appl. Phys.*, **76**, 4192-4200, 1994.
2. "Kinetics of $\text{Si}_{1-x}\text{Ge}_x/\text{Si}$ ($0 \leq x \leq 1$) Growth by Molecular Beam Epitaxy Using Disilane and Germanium", F.C. Zhang, J. Singh and P. Bhattacharya, *Applied Physics Lett.*, **67**, 85, 1995.
3. "Surface Phenomena and Kinetics of $\text{Si}_{1-x}\text{Ge}_x/\text{Si}$ ($0 \leq x < 1$) Growth By Molecular Beam Epitaxy Using Si_2H_6 and Ge/GeH_4 ", F.C. Zhang, J. Singh and P. Bhattacharya, submitted to the Fifteenth North American Conference on Molecular Beam Epitaxy, University of Maryland at College Park, September 17-20, 1995.
4. "Surface Phenomena and Kinetics of $\text{Si}_{1-x}\text{Ge}_x/\text{Si}$ ($0 \leq x < 1$) Growth By Molecular Beam Epitaxy Using Si_2H_6 and Ge/GeH_4 ", F.C. Zhang, J. Singh and P. Bhattacharya, *J. Vac. Sci. Technology. B*, **14**(3), 2378-2380, May/June 1996.
5. "Responsivity and Impact Ionization Coefficients of $\text{Si}_{1-x}\text{Ge}_x$ Photodiodes", J. Lee, A.L. Gutierrez-Aitken, S.H. Li and P. Bhattacharya, *IEEE Transactions on Electron Devices*, **43**, No. 6, 977-981, June 1996.
6. "The Effect of Strain on Hot-Electron and Hole Longitudinal Diffusion Noise in Si and $\text{Si}_{0.9}\text{Ge}_{0.1}$ ", K. Yeom, J.M. Hinckley and J. Singh, *J. Appl. Phys.*, **78**, 5454, 1995.
7. "High Field Thermal Noise of Holes in Silicon: The Effect of Valence Band Anisotropy", J.M. Hinckley and J. Singh, *J. Appl. Phys.* **80** (12), 6766, 1996.
8. "Laser Induced Impact Ionization in Semiconductors; A Monte Carlo Study", B. Kockman, K. Yeom and J. Singh, *Appl. Phys. Lett.*, **68**, 1936, 1996.
9. "Transverse Velocity Fluctuation Autocorrelation Function of Holes in Silicon: The Effect of Valence-Band Anisotropy", J.M. Hinckley and J. Singh, *Phys. Rev. B.*, **51** (15), 9648, 1995.
10. "Anisotropic High-Field Transverse Differential Mobility of Holes in Silicon", J.M. Hinckley and J. Singh, *Appl. Phys. Lett.*, **67**, 2966, 1995.
11. "Calculation of Electron and Hole Impacts Ionization Coefficients in SiGe Alloys", K. Yeom, J.M. Hinckley and J. Singh, *J. Appl. Phys.*, **80** (12), 6773, 1996.
12. "Free Carrier Absorption as a Probe of Carrier Dynamics: A Monte Carlo Based Study for Silicon", H. Jiang, J.M. Hinckley and J. Singh, *Appl. Phys. Lett.*, **70**(14), 1834, 1997.
13. "High Power Laser Semiconductor Interactions: A Monte Carlo Study for Silicon", K. Yeom, H. Jiang and J. Singh, *J. Appl. Phys.*, **81** (4), 1807, 1997.
14. "Characterization of Mismatched SiGe Grown on Low Temperature Si Buffer Layers by Molecular Beam Epitaxy", K.K. Linder, F.C. Zhang, J.S. Rieh and P. Bhattacharya, *9th International Conference on Molecular Beam Epitaxy*, Malibu, California, August, 1996.

15. "Reduction of Dislocation Density in Mismatched SiGe/Si Using a Low-Temperature Si Buffer Layer", K.K. Linder, F.C. Zhang, J.-S. Rieh, P. Bhattacharya and D. Houghton, *Appl. Phys. Lett.*, **70** (24), 3224, 1997.
16. "Very High ($>10^{19} \text{ cm}^{-3}$) *in situ* n-type Doping of Silicon During Molecular Beam Epitaxy Using Supersonic Jets of Phosphine", R. Malik, E. Gulari, P. Bhattacharya, K.K. Linder and J.-S. Rieh, *Appl. Phys. Lett.*, **70** (9), 1149, 1997.
17. "Characterization of Mismatched SiGe Grown on Low Temperature Si Buffer Layers by Molecular Beam Epitaxy", K.K. Linder, F.C. Zhang, J.S. Rieh and P. Bhattacharya, *J. Crystal Growth*, **175**, May, 1997.
18. "High-field Thermal Noise of Holes in Silicon: The Effect of Valence Band Anisotropy", J.M. Hinckley and J. Singh, *J. Appl. Phys.*, **80** (12), 6766, 1996.
19. "Calculation of Electron and Hole Impact Ionization Coefficients in SiGe Alloys", K. Yeom, J.M. Hinckley and J. Singh, *J. Appl. Phys.*, **80** (12), 6773, 1996.
20. "Carrier Dynamics Studies Through Free-Carrier Absorption: A Monte Carlo Study for Silicon", H. Jiang, J.M. Hinckley and J. Singh, *J. Quantum. Elect.*, **33**, 1779, October 1997.
21. "Single- and Dual-Feedback Transimpedance Amplifiers Implemented by SiGe HBT Technology", J.-S. Rieh, O. Qasaimeh, L.H. Lu, K. Yang, L.P.B. Katehi, P. Bhattacharya and E.T. Croke, *IEEE Mecrowave and Guided Wave Letters*, **8**, No. 2, 1998.
22. "Electro-Absorption and Electro-Optic Effect in SiGe/Si Quantum Wells: Realization of Low-Voltage Optical Modulators", O. Qasaimeh, J. Singh and P. Bhattacharya, *J. Quantum Electron.*, **33**, 1532-1536, 1997.
23. "Monolithically Integrated SiGe/Si PIN-HBT Front-End Photoreceivers", *Photon. Tech. Letts.*, accepted for publication.
24. "Monolithically Integrated SiGe/Si PIN-HBT Front-End Transimpedance Photoreceivers", presented at *IEEE/Cornell Biennial Conference*, Ithaca, New York, August 1997.
25. "SiGe/Si Quantum Well Electroabsorption Modulators", *Photon. Tech. Letts.*, accepted for publication.
26. "Channel Effective Mass and Interfacial Effects in P-MOSFET: a 6-band $\mathbf{k} \cdot \mathbf{p}$ Charge Control Study", Y. Zhang and J. Singh, submitted to *Phys. Rev. B*, December 1997.

PERSONNEL SUPPORTED BY AND ASSOCIATED WITH PROJECT

Faculty: P. Bhattacharya
E. Gulari
J. Singh

Post-Doctoral Fellows: Dr. J. Hinckley
Dr. K. Kamath
Dr. F-C. Zhang

Graduate Students: J. Lee (graduated 5/96)
K. Linder
R. Malik (graduated 7/96)
J-S. Rieh